The Evolution of Gas-Phase Metallicity and Resolved Abundances in Star-forming Galaxies at $z \approx 0.6 - 1.8$

S. Gillman [1,2,3]★　A. L. Tiley [1,4]　A. M. Swinbank [1]　U. Dudzevičiūtė [1]

R. M. Sharples [1,5]　Ian Smail [1]　C. M. Harrison [6]　Andrew J. Bunker [7,8]

Martin Bureau [7]　M. Cirasuolo [9]　Georgios E. Magdis [2,3,10,11]

Trevor Mendel [12] and John P. Stott [13]

[1]*Centre for Extragalactic Astronomy, Durham University, South Road, Durham, DH1 3LE UK*
[2]*Cosmic Dawn Center (DAWN), Copenhagen, Denmark*
[3]*DTU-Space, Technical University of Denmark, Elektrovej 327, DK-2800 Kgs. Lyngby, Denmark*
[4]*International Centre for Radio Astronomy Research, University of Western Australia, 35 Stirling Highway, Crawley, WA, Australia*
[5]*Centre for Advanced Instrumentation, Durham University, South Road, Durham DH1 3LE UK*
[6]*School of Mathematics, Statistics and Physics, Newcastle University, Newcastle upon Tyne NE1 7RU, UK*
[7]*Sub-department of Astrophysics, Department of Physics, University of Oxford, Denys Wilkinson Building, Keble Road, Oxford OX1 3RH, UK*
[8]*Kavli Institute for the Physics and Mathematics of the Universe (WPI), The University of Tokyo, Kashiwa, Chiba 277-8583, Japan*
[9]*European Southern Observatory, Karl-Schwarzschild-Str 2, D-86748 Garching b. München, Germany*
[10]*University of Copenhagen, Lyngbyvej 2, DK-2100 Copenhagen Ø, Denmark*
[11]*Institute for Astronomy, Astrophysics, Space Applications and Remote Sensing, National Observatory of Athens, GR-15236 Athens, Greece*
[12]*Research School of Astronomy and Astrophysics, Australian National University, Canberra, ACT 2611, Australia*
[13]*Department of Physics, Lancaster University, Bailrigg, Lancaster LA1 4YB, UK*

ABSTRACT

We present an analysis of the chemical abundance properties of $\approx$650 star-forming galaxies at $z \approx 0.6 - 1.8$. Using integral-field observations from the K-band Multi-Object Spectrograph (KMOS), we quantify the [NII]/Hα emission-line ratio, a proxy for the gas-phase Oxygen abundance within the interstellar medium. We define the stellar mass $-$ metallicity relation at $z \approx 0.6 - 1.0$ and $z \approx 1.2 - 1.8$ and analyse the correlation between the scatter in the relation and fundamental galaxy properties (e.g. Hα star-formation rate, Hα specific star-formation rate, rotation dominance, stellar continuum half-light radius and Hubble-type morphology). We find that for a given stellar mass, more highly star-forming, larger and irregular galaxies have lower gas-phase metallicities, which may be attributable to their lower surface mass densities and the higher gas fractions of irregular systems. We measure the radial dependence of gas-phase metallicity in the galaxies, establishing a median, beam smearing-corrected, metallicity gradient of $\Delta Z/\Delta R = 0.002 \pm 0.004$ dex kpc^{-1}, indicating on average there is no significant dependence on radius. The metallicity gradient of a galaxy is independent of its rest-frame optical morphology, whilst correlating with its stellar mass and specific star-formation rate, in agreement with an inside-out model of galaxy evolution, as well as its rotation dominance. We quantify the evolution of metallicity gradients, comparing the distribution of $\Delta Z/\Delta R$ in our sample with numerical simulations and observations at $z \approx 0 - 3$. Galaxies in our sample exhibit flatter metallicity gradients than local star-forming galaxies, in agreement with numerical models in which stellar feedback plays a crucial role redistributing metals.

Key words: galaxies: abundances – galaxies: high-reshift – galaxies: kinematics and dynamics

1 INTRODUCTION

The ejection of metals into the interstellar medium via winds from massive stars in the asymptotic giant branch phase or via supernovae

★ E-mail: srigi@space.dtu.dk

acts to increase the chemical abundance in star-forming galaxies. This influx of metals is mediated by inflows, outflows and cold gas accretion (e.g. Köppen & Edmunds 1999; Calura & Matteucci 2006; Erb 2008; Steidel et al. 2010; Davé et al. 2012; Lu et al. 2015; Sanders et al. 2015; Anglés-Alcázar et al. 2017; Christensen et al. 2018; Sanders et al. 2018). Empirically constraining the complex interplay between these secular processes and their imprint on the chemical abundance properties of galaxies is crucial to fully constrain the baryon cycle.

In the local Universe, the correlation between a galaxy's stellar mass (M_*) and its integrated gas-phase metallicity (Z), the mass−metallicity relation, has been well studied (e.g. Lequeux et al. 1979; Tremonti et al. 2004). Higher stellar mass star-forming galaxies have been shown to exhibit higher gas-phase metallicities at $z \approx 0$ with $Z \propto M_*^{2/5}$ up to $M_* \sim 10^{10} M_\odot$, above which the relation saturates to a constant metallicity. This strong correlation between stellar mass and metallicity is believed to be a consequence of supernovae driven winds and outflows which remove the metal-rich gas from the interstellar medium (e.g. Tremonti et al. 2004; Tumlinson et al. 2011). In lower stellar mass galaxies, with shallower potential wells, a larger fraction of this material is removed from the galaxy resulting in an overall lower metallicity (e.g. Arimoto & Yoshii 1987; Garnett 2002; Brooks et al. 2007; Chisholm et al. 2018). Higher stellar mass galaxies are also believed to evolve more rapidly at higher redshifts and have therefore converted more of their pristine gas into stars and metals, resulting in higher gas-phase metallicities (e.g. Maiolino et al. 2008; Somerville & Davé 2015; Sanders et al. 2018).

The star-formation rate and gas fraction of a galaxy have also been linked to its offset from the mass−metallicity relation, with suggestions of the existence of a fundamental metallicity plane. In this plane, more highly star-forming galaxies, at a given stellar mass, have lower gas-phase metallicities (e.g. Mannucci et al. 2010; Sánchez et al. 2017b; Sánchez-Menguiano et al. 2019). Surveys of galaxies in the local Universe, such as Calar Alto Legacy Integral Field Area Survey (CALIFA; Sánchez et al. 2012) and Mapping Nearby Galaxies at Apache Point Observatory (MaNGA; Bundy et al. 2015), which observed thousands of galaxies out to $z \approx 0.03$, have shown a correlation between galaxy star-formation rate and offset from the mass−metallicity relation (e.g. Sánchez Almeida & Sánchez-Menguiano 2019; Cresci et al. 2019).

Attempts have been made to define the mass−metallicity relation (and plane) in the distant Universe. The ratio of strong optical nebular metal emissions lines to the Balmer series (e.g. [Nɪɪ]/Hα) is commonly used to infer the gas-phase metallicity of galaxies at high redshift due to their spectral proximity, making them insensitive to dust and observable from ground-based facilities (e.g. Yabe et al. 2015; Wuyts et al. 2016; Förster Schreiber et al. 2018; Curti et al. 2020b).

The ratio is often expressed as an Oxygen abundance relative to Hydrogen, as Oxygen is generally the most abundant heavy element by mass and therefore provides a proxy for the metallicity of the galaxy (Pettini & Pagel 2004). Using these strong-line calibrations of optical emission lines, many recent studies have shown that the mass−metallicity relation evolves above $z = 1$, with higher-redshift galaxies having lower metallicities at a given stellar mass (e.g. Erb et al. 2006; Maiolino et al. 2008; Zahid et al. 2011; Stott et al. 2013; Yabe et al. 2015; Wuyts et al. 2016; Sanders et al. 2018).

Despite evolution in the normalisation of the mass−metallicity relation, it has been suggested that the fundamental plane of stellar mass, gas-phase metallicity and star-formation rate does not evolve with cosmic time. For example Mannucci et al. (2011) proposed that the evolution in the mass−metallicity relation comes from sampling

different regions of the non-evolving fundamental plane, given the higher average star formation at earlier cosmic times (Cresci et al. 2019). To confirm this result, metallicity measurements of large samples of high-redshift galaxies are required, which has recently been made possible with the advent of high-redshift multi-object spectroscopy.

Using the MOSFIRE Deep Evolution Field (MOSDEF) Survey, Sanders et al. (2015, 2018) demonstrated the presence of the relation between stellar mass, metallicity and star−formation rate in 260 galaxies at $z \approx 2.3$. However the star-forming galaxies in the MOSDEF survey exhibit ≈ 0.1 dex lower metallicity than local galaxies, at fixed stellar mass and star-formation rate. Sanders et al. (2018) concludes that there is not a fundamental plane that can simultaneously match the properties of star-forming galaxies in both the local and distant Universes. This implies that the metallicity properties of the interstellar medium of star-forming galaxies evolves with cosmic time.

As well as the galaxy integrated metallicity, the distribution of metals within a galaxy provides insights into the influence of star formation, gas accretion, mergers and feedback, that all play a key role in defining the evolution of galaxies. In the local Universe most isolated galaxies exhibit negative log-linear abundance gradients (i.e metallicity decreasing with radius). Higher gas-phase metallicities are observed in the central regions of the galaxies where star formation is most prevalent and supernovae enrich the surrounding interstellar medium (e.g. Sánchez et al. 2014; Kaplan et al. 2016; Poetrodjojo et al. 2018). The observed negative gradients are predicted from inside-out theories for the growth of galaxy discs (e.g. Boissier & Prantzos 1999) and are well modelled in hydrodynamical simulations such as Evolution and Assembly of GaLaxies and their Environments (EAGLE) (e.g. De Rossi et al. 2017; Collacchioni et al. 2020).

At high redshift the picture is much less clear, with various observational studies reporting a range of metallicity gradients in isolated star-forming galaxies (e.g. Cresci et al. 2010; Jones et al. 2010; Swinbank et al. 2012; Jones et al. 2013; Stott et al. 2014; Leethochawalit et al. 2016; Wuyts et al. 2016; Molina et al. 2017; Wang et al. 2017; Curti et al. 2020b) as well as in simulations (e.g Pilkington et al. 2012; Anglés-Alcázar et al. 2014; Finlator 2017; Sillero et al. 2017; Collacchioni et al. 2020; Hemler et al. 2020). In this paper, we exploit a large sample of high-redshift star-forming galaxies with spatially-resolved metallicity profiles. Utilizing the strong-line calibration of the [Nɪɪ]/Hα ratio, we present an analysis of the gas-phase metallicity properties of ≈ 650 star-forming galaxies in the redshift range $z \approx 0.6 - 1.8$. We explore the correlations between galaxy morphology, dynamics and position on the mass−metallicity relation, as well as the metallicity profile of the galaxies.

This paper is organized as follows. In Section 2 we describe the observations and sample selection. We define the procedure used to correct for the galaxies velocity fields and de-redshift the integral-field data, from which we extract the gas-phase metallicities. In Section 3 we present the mass−metallicity relation and fundamental metallicity plane of the sample. We analyse the radial dependence of metallicity and its correlation with galaxy dynamics, morphology and redshift in Section 4, before presenting our conclusions in Section 5.

A nine-year *Wilkinson Microwave Anisotropy Probe* (Hinshaw et al. 2013) cosmology is used throughout this work with $\Omega_\Lambda = 0.721$, $\Omega_m = 0.279$ and $H_0 = 70\,\mathrm{km\,s^{-1}\,Mpc^{-1}}$. In this cosmology an angular resolution of 0.70 arcsecond (the median full width half maximum (FWHM) of the seeing in our data) corre-
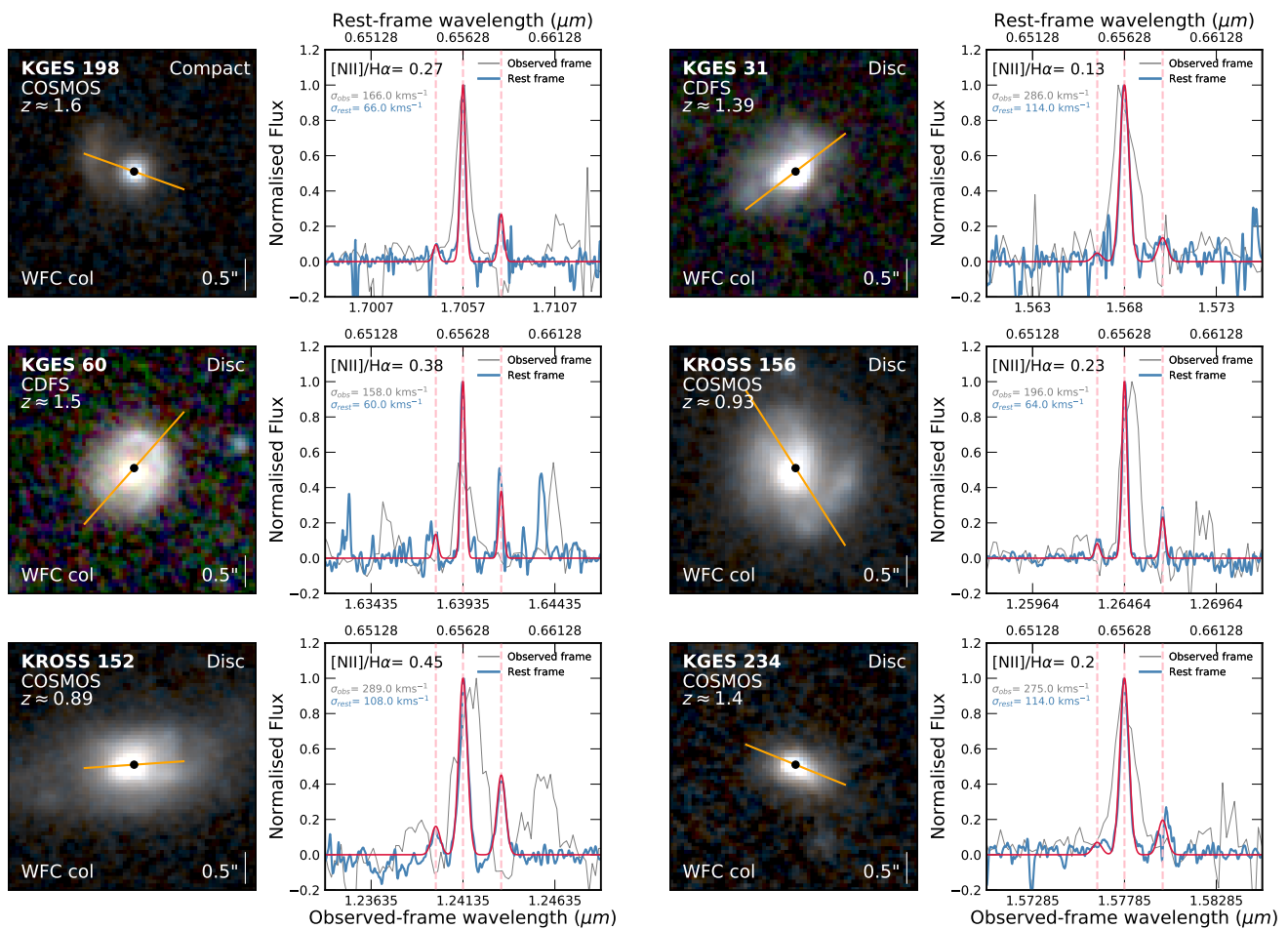
Figure 1. Example *HST* images and integrated spectra of galaxies in our sample. For each galaxy we show a WFC3 three-colour image composed of F105W, F125W and F160W images. The semi-major axis of the galaxy (orange line) and stellar continuum centre (black filled circle) are indicated, as well as the morphological class if available from the Huertas-Company et al. (2015) classification. The galaxy integrated spectra from the observed KMOS data cube (grey) and de-redshifted rest-frame cube with bulk motions removed (blue) are also shown. The Hα and [NII] emission lines are indicated (vertical pink dashed lines) and we overlay the spectral fit to the de-redshifted and corrected emission lines (crimson line). The [NII]/Hα ratio of each galaxy, as well as the velocity dispersion of the spectra are indicated in the top left. The examples show a range of [NII]/Hα ratio from galaxies with varying morphologies and redshifts.

sponds to a physical scale of 5.5 kpc at a redshift $z = 0.91$ (the median redshift of our data). All quoted magnitudes are in the AB system and stellar masses are calculated assuming a Chabrier initial mass function (IMF) (Chabrier 2003).

2 SAMPLE SELECTION AND ANALYSIS

To provide statistically meaningful conclusions about the metallicities of galaxies in the distant Universe, we utilize 644 star-forming galaxies drawn from two large K-band multi-object spectrograph (KMOS; Sharples et al. 2004, 2013) programmes at $z \approx 0.6 - 1.8$. The galaxies in our sample are drawn from the KMOS Redshift One Spectroscopic Survey (KROSS; Stott et al. 2016; Harrison et al. 2017) at $z \approx 0.6 - 1.0$ (448 galaxies) and the KMOS Galaxy Evolution Survey (KGES; Gillman et al. 2019, Tiley et al. in prep.) at $z \approx 1.2 - 1.8$ (196 galaxies).

All the galaxies in the sample were observed using KMOS, a multi-object spectrograph mounted on the Nasmyth focus of the 8-m class UT1 telescope at the VLT, Chile. It has 24 individual integral-field units that patrol a 7.2 arcminute diameter field, each with a 2.8×2.8 arcsecond^2 field of view and 0.2×0.2 arcsecond^2

spaxels. KMOS utilizes image slices to produce data cubes with wavelength coverages of $0.8 - 1.0$, $1.0 - 1.4$, $1.4 - 1.9$, $1.9 - 2.5$ or $1.5 - 2.5 \mu m$ in the *IZ*, *YJ*, *H*, *K* or *HK* band respectively. In the following sections we provide an overview of the KROSS and KGES surveys.

2.1 KROSS

KROSS is a KMOS survey of 795 typical star-forming galaxies in the redshift range $z \approx 0.6 - 1.0$ selected from the Extended *Chandra* Deep Field South (E-CDFS; Giacconi et al. 2001), Cosmological Evolution Survey (COSMOS; Scoville et al. 2007), UKIRT Infrared Deep Sky Survey (UKIDSS) Ultra-Deep Survey (UDS; Lawrence et al. 2007) and the SA22 (Lilly et al. 1991; Steidel et al. 1998) extragalactic fields. The majority of the sample galaxies are selected using archival spectroscopic redshifts, 25 per cent being Hα narrow-band emitters at $z = 0.84$ from the High Redshift Emission Line Survey (HiZELS) and Canada-France HiZELS (CF-HIZELS) surveys (Sobral et al. 2013, 2015). A full description of the KROSS survey and derived galaxy properties is given in Stott et al. (2016) and Harrison et al. (2017).
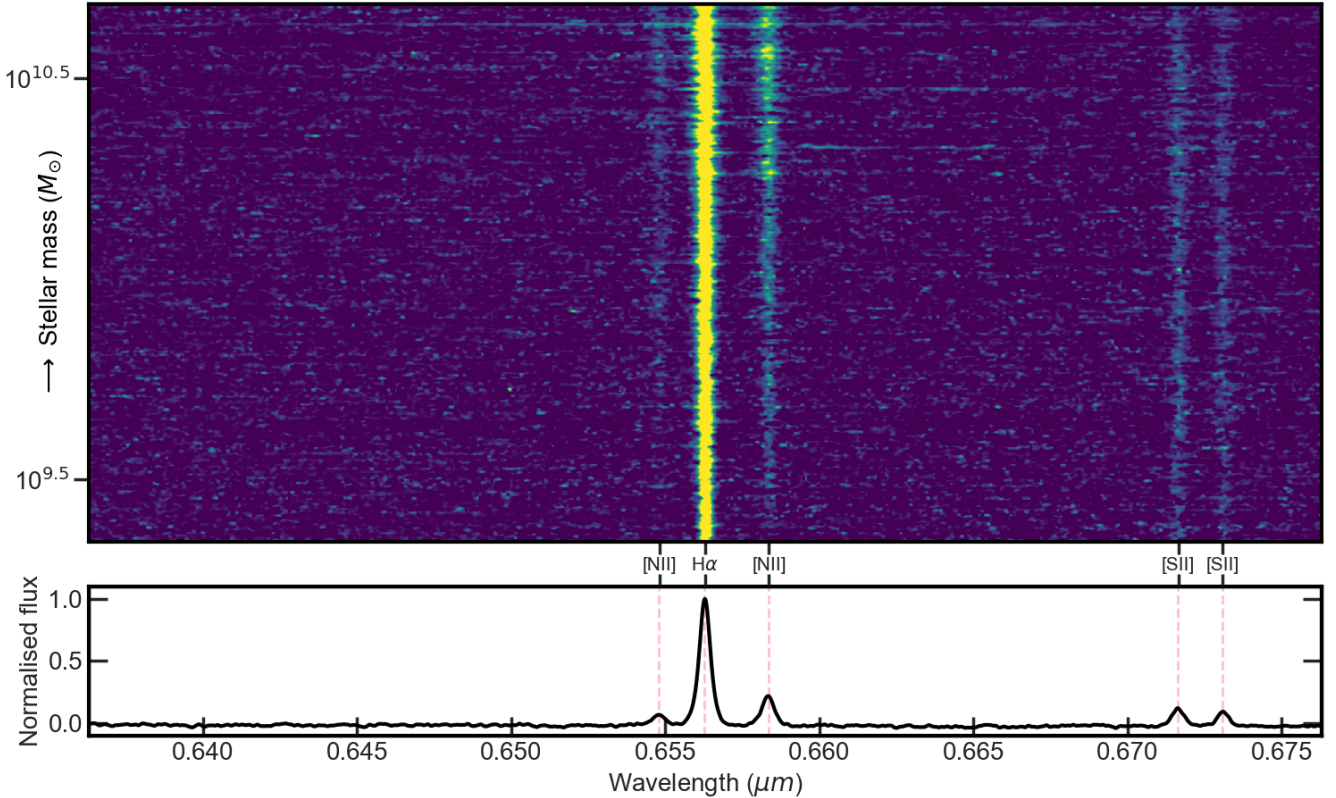
Figure 2. Top: Spectra of all 644 spatially-resolved KMOS galaxies, with the de-redshifting and velocity correction procedure applied, ranked by stellar mass. The spectra of the higher stellar mass galaxies reveal the weaker [NII] forbidden emission lines whilst the stronger recombination emission line (Hα) and [SII] forbidden emission line are present in all galaxies. This reflects the increase of the gas-phase metallicity with stellar mass seen in the mass – metallicity relation. **Bottom**: Normalised stacked spectrum over all 644 KMOS observations, with both forbidden and recombination emission lines indicated (vertical pink dashed lines).

The KROSS targets were predominantly selected to have bright Hα emission in the *J*-band, avoiding OH skylines, and a total apparent magnitude $K < 22.5$, with a 'blue' colour $r - z < 1.5$. Of the 795 galaxies targeted, 586 were detected in Hα emission. Removing galaxies with [NII]/H$\alpha > 0.8$ and/or a $\gtrsim 1000$ km s^{-1} broad-line component in the Hα emission-line profiles, indicating the presence of an active galactic nucleus (AGN), leaves 448 galaxies, for which we can measure the gas-phase metallicities. These 448 galaxies of the KROSS sample have a median stellar mass of $\log(M_*[M_\odot]) = 10.0$ with a $16 - 84$th percentile range of $\log(M_*[M_\odot]) = 9.6 - 10.4$ as derived using the HYPERZ (Bolzonella et al. 2000) spectral energy distribution (SED) fitting code. The dust-corrected Hα star-formation rates of the sample are derived following Kennicutt (1998), corrected to a Chabrier initial mass function and assuming a median Hα extinction, calculated from SED fitting, of $A_{H\alpha} = 1.73$. The $z \approx 0.6 - 1.0$ sample has a median value, and bootstrap uncertainty, of SFR $= 7 \pm 1$ M$_\odot$ yr^{-1} with a $16 - 84$th percentile range of SFR $= 4 - 15$ M$_\odot$ yr^{-1} (see Stott et al. 2016 and Harrison et al. 2017 for details).

2.2   KGES

KGES is a KMOS survey that targets 288 star-forming galaxies at $z \approx 1.2 - 1.8$ that preferentially lie within some of the Cosmic Assembly Near-infrared Deep Extragalactic Legacy Survey (CAN-DELS; Grogin et al. 2011) *Hubble Space Telescope* (*HST*) fields. The programme probes ongoing star formation in the galaxies using the Hα and [NII] emission lines. Galaxies with a *K*-band magnitude of $K < 22.5$ are selected from the UDS, COSMOS and E-CDFS extragalactic fields. No prior morphological selection was made, with the remaining KMOS integral field unit (IFU) arms filled with fainter galaxies. Of the 288 galaxies targeted, 243 were detected in Hα emission and 235 have spatially-resolved Hα emission.

We remove potential AGN from the sample using the galaxies' infrared colours, following the Donley et al. (2012) and Stern et al. (2012) colour selection, and exclude galaxies with X-ray counterparts. We also remove galaxies with [NII]/H$\alpha > 0.8$ (see Tiley et al. in prep. for details) and galaxies with no [NII] detection. This leaves 196 galaxies in which we can measure the integrated [NII]/Hα ratio. These 196 galaxies of the KGES sample have a median stellar mass of $\log(M_*[M_\odot]) = 10.0$ with a $16-84$th percentile range of $\log(M_*[M_\odot]) = 9.6 - 10.6$ as derived using the MAGPHYS SED fitting code (Gillman et al. 2019). We note that the MAGPHYS SED fitting code is different to the HYPERZ code used for the KROSS galaxies, which can lead to up a 0.3 dex systematic discrepancy in stellar mass estimates (e.g. Mobasher et al. 2015). The dust-corrected Hα star-formation rate are calculated following the methods of (Wuyts et al. 2013) assuming a Calzetti et al. (1994) extinction law (see Tiley et al. in prep.). The median dust-corrected Hα star-formation rate, and bootstrap uncertainty, of the sample is SFR $= 20 \pm 1$ M$_\odot$ yr^{-1} with a $16 - 84$th percentile range of SFR $= 8 - 45$ M$_\odot$ yr^{-1}.

We combine both the KROSS and KGES samples to create a sample of 644 star-forming galaxies at $z \approx 0.6 - 1.8$ for which we

can measure the gas-phase metallicities as traced by the [NII]/Hα ratios. In Figure 1 we show examples of the galaxies in our sample, highlighting the range of rest-frame optical morphologies and [NII]/Hα ratios.

2.3   De-redshifting and correcting for velocity gradient

The integrated spectrum of a galaxy contains information about its intrinsic emission-line properties. Any emission or absorption feature in the spectrum is broadened by motions along the line-of-sight. However, with integral-field data it is possible to model the two-dimensional velocity field and correct for this dynamical broadening, as we describe in this section.

For each spectrum within the datacube of a galaxy, we re-normalise the spectrum using the spectroscopic redshift of the galaxy such that the Hα emission line of the continuum centre, determined from broadband imaging, is centred at the rest-frame wavelength of Hα, $\lambda 6563$ Å. Using the Hα velocity map, as derived in Harrison et al. (2017) and Tiley et al. (in prep.), we then shift each spaxel's spectrum to correct for the mean velocity at that spaxel, estimated from the velocity field of the galaxy. We note that the velocity field is derived using an adaptive binning technique on the datacube with a spaxel Hα signal-to-noise (S/N) threshold of S/N≥ 5 (see Harrison et al. 2017, Tiley et al. in prep. for details). This velocity field thus defines the aperture in which we later calculate the de-redshifted integrated spectrum of the galaxy. Any spaxels outside of the velocity map (i.e. S/N<5) are excluded as we do not have a velocity correction for these spaxels.

To confirm the de-redshifting process has removed the broadening of the emission lines due to the spaxel to spaxel variation in the Hα velocity in each galaxy, we measure the velocity dispersion of each galaxy's integrated spectrum before and after de-redshifting. We note we do not account for the line broadening due to the velocity gradient within each individual spaxel. The observed Hα emission lines of the $z \approx 0.6 - 1.0$ galaxies have a median velocity dispersion of $\sigma_{\rm gal} = 162 \pm 4$ km s^{-1} with a 16th$-$84th percentile range of $\sigma_{\rm gal} = 106 - 258$ km s^{-1}. At $z \approx 1.2 - 1.8$ the galaxies have a median velocity dispersion of $\sigma_{\rm gal} = 246 \pm 9$ km s^{-1} with a 16th$-$84th percentile range of $\sigma_{\rm gal} = 165 - 381$ km s^{-1}. After de-redshifting, the median velocity dispersion of the $z \approx 0.6 - 1.0$ sample is $\sigma_{\rm gal} = 82 \pm 2$ km s^{-1} with a 16th$-$84th percentile range of $\sigma_{\rm gal} = 61 - 127$ km s^{-1} whilst the $z \approx 1.2 - 1.8$ galaxies have a median of $\sigma_{\rm gal} = 85 \pm 2$ km s^{-1} with a 16th$-$84th percentile range of $\sigma_{\rm gal} = 66 - 114$ km s^{-1}. This demonstrates the effect of removing bulk motions within the galaxy (see Figure 1).

We apply this de-redshifting procedure to all 644 KMOS data cubes in our sample. To measure the [NII]/Hα ratio in each galaxy, we first generate an integrated spectrum by spatially collapsing the de-redshifted data cubes. In Figure 2 we show the integrated spectra of all galaxies ranked by stellar mass. The Hα emission line and [SII] forbidden lines are prominent in all galaxies, whilst the [NII] forbidden transition lines at $\lambda 6548$Å and $\lambda 6583$Å are more prominent in higher stellar mass galaxies. This reflects the increase of the gas-phase metallicity with stellar mass seen in the mass$-$metallicity relation (e.g. Tremonti et al. 2004; Mannucci et al. 2010).

3   MASS$-$METALLICITY RELATION

To measure the gas-phase metallicity in our sample, we utilize the [NII]/Hα emission line ratio both as an integrated quantity and as a function of radius.

We model the Hα and [NII] emission lines using three Gaussian profiles with fixed wavelength offsets and coupled FWHMs, following the same procedure as the emission-line fitting in Gillman et al. (2019). The fitting procedure uses a five parameter model with continuum, Hα peak intensity, line center, line width, and [NII]/Hα ratio. We apply this fitting procedure to all observed galaxies with an Hα integrated line flux S/N > 5. We derive a median [NII]/Hα ratio for the $z \approx 0.6 - 1.0$ galaxies of [NII]/H$\alpha = 0.25 \pm 0.01$ with a 16th$-$84th percentile range of [NII]/H$\alpha = 0.10 - 0.42$. Whilst the $z \approx 1.2 - 1.8$ galaxies have a median value of [NII]/H$\alpha = 0.19 \pm 0.02$ with a 16th$-$84th percentile range of [NII]/H$\alpha = 0.10 - 0.37$. In the local Universe a galaxy's gas-phase metallicity correlates strongly with other fundamental properties (e.g. stellar mass, star-formation rate, morphology) (e.g. Tremonti et al. 2004; Ellison et al. 2008; Sánchez-Menguiano et al. 2019). In the next section, we analyse these correlations in our high-redshift sample of 644 star–forming galaxies.

3.1   The mass$-$metallicity relation

To quantify the processes that drive the baryon cycle within galaxies and ultimately drive their evolution, we analyse the connection between the metal content of the interstellar medium (e.g. gas-phase metallicity) and other fundamental galaxy properties such as stellar mass and star-formation rate.

To analyse the mass$-$metallicity relation at high redshift, we show the galaxy integrated [NII]/Hα ratio as a function of stellar mass in Figure 3 for both the $z \approx 0.6 - 1.0$ and $z \approx 1.2 - 1.8$ samples. We convert the [NII]/Hα ratio to an Oxygen abundance using the linear conversion from Pettini & Pagel (2004), of the form,

$$12 + \log(\rm O/H) \; = \; 8.90 + 0.57 \log([\rm NII]/H\alpha), \qquad (1)$$

which has a systematic uncertainty of 0.18 dex. The median gas-phase metallicity of galaxies at $z \approx 0.6 - 1.0$ is $12 + \log(\rm O/H) = 8.56 \pm 0.01$ with a $16 - 84$th percentile range of $12 + \log(\rm O/H) = 8.34 - 8.69$. For the $z \approx 1.2 - 1.8$ sub-sample the median metallicity is $12 + \log(\rm O/H) = 8.49 \pm 0.02$ with a $16 - 84$th percentile range of $12 + \log(\rm O/H) = 8.32 - 8.65$.

Higher stellar mass galaxies in our sample generally have higher metallicities, with a weaker dependence on stellar mass at the highest masses. This is in agreement with other high-redshift studies of galaxies (e.g. Stott et al. 2013; Yabe et al. 2015; Wuyts et al. 2016; Förster Schreiber et al. 2018; Sanders et al. 2018; Curti et al. 2020a), as well as inside-out galaxy evolution models and hydrodynamical simulations that predict feedback-driven winds and outflows which remove metal-rich material from lower-mass galaxies more easily than higher-mass systems, due to the their shallower potential wells (e.g. De Rossi et al. 2017; Anglés-Alcázar et al. 2017; Chisholm et al. 2018; Gao et al. 2018).

In Figure 3 we overlay on our data trends from observations of low-redshift galaxies ($z \approx 0$) from Curti et al. (2020a) as well as high-redshift ($z \approx 1.4 - 2.7$) galaxies from the Fiber-Multi Object Spectrograph (FMOS) survey (Zahid et al. 2014). We note due to the different SED fitting codes used in the comparison samples there can be systematic offsets in stellar mass estimates (see Mobasher et al. 2015). On average the $z \approx 0.6 - 1.0$ sample is offset by 0.15 ± 0.05 dex to lower metallicities compared to the $z \approx 0$ star-
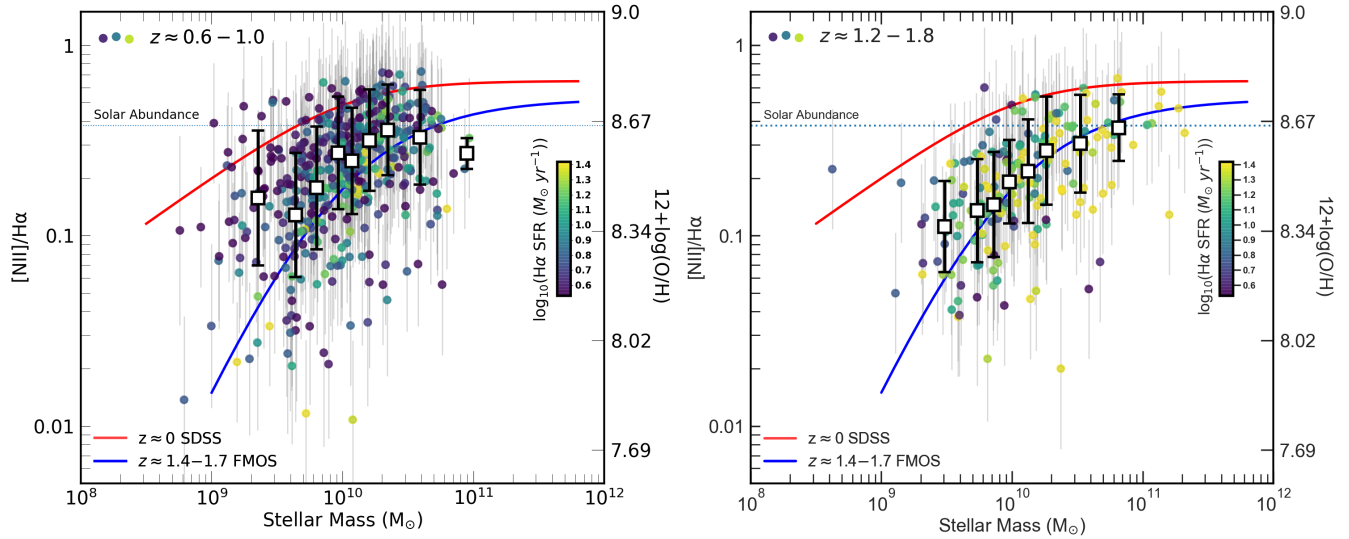
Figure 3. Galaxy integrated gas-phase metallicity, measured from the integrated [NII]/Hα ratio, as a function of stellar mass, coloured by the galaxy dust-corrected Hα star-formation rate, for both $z \approx 0.6 - 1.0$ galaxies (**left**) and $z \approx 1.2 - 1.8$ galaxies (**right**). The red line represents the mass $-$ metallicity relation at $z \approx 0$ derived from Sloan Digital Sky Survey (SDSS) (Curti et al. 2020a) whilst the blue line indicates the mass $-$ metallicity relation at $z \approx 1.4 - 1.70$ from the Fiber-Multi Object Spectrograph (FMOS) survey (Zahid et al. 2014). The horizontal dashed line indicates solar metallicity ($12 + \log(\text{O/H}) = 8.66$; Asplund 2005). The metallicity is converted from a [NII]/Hα ratio to an Oxygen abundance following the linear calibration of Pettini & Pagel (2004). The black squares (and error bars) indicate a running median and 1-σ scatter, an interpolation of which is used to derive the offset from the median mass $-$ metallicity relation (ΔZ). In both redshift slices, higher stellar mass galaxies have higher metallicities, with an indication that more highly star-forming galaxies have lower gas-phase metallicities at a given stellar mass. The lower redshift $z \approx 0.6 - 1.0$ galaxies generally have higher metallicities than $z \approx 1.2 - 1.8$ galaxies, in agreement with the evolution between the $z \approx 1.4 - 2.7$ and $z \approx 0$ observations. Note the limit [NII]/H$\alpha < 0.8$ at $z \approx 0.6 - 1.0$ and $z \approx 1.2 - 1.8$ to remove AGN, which are predominantly higher stellar mass galaxies.

forming galaxies from Curti et al. (2020a), whilst the $z \approx 1.2 - 1.8$ sample is offset by 0.22 ± 0.05 dex. Both samples have comparable metallicities to the $z \approx 1.4 - 2.7$ galaxies analysed by Zahid et al. (2014). We note if we include galaxies with [NII]/H$\alpha >= 0.8$ the median trend at $z \approx 0.6 - 1.0$ increases on average by 0.03 dex whilst the $z \approx 1.2 - 1.8$ median track is unaffected.

The gas-phase metallicities of our sample galaxies agrees with the evolution of the mass $-$ metallicity relation identified by other surveys of star-forming galaxies (e.g. Sanders et al. 2018; Huang et al. 2019). It has been proposed that this evolution could be explained by the lower metallicity of infalling gas at higher redshift and an increase in the mass loading factor of outflows and winds, that remove metal-enriched gas from the interstellar medium. Other studies suggest this evolution maybe driven by the redshift evolution of star formation efficiency (e.g. Lilly et al. 2013), outflow strength (e.g. Lian et al. 2018; Sanders et al. 2020), and gas fraction (e.g. Sanders et al. 2020). Lower than expected metallicities in high-redshift galaxies may also be related to the increased likelihood of galaxy interactions in the distant Universe (e.g. Bustamante et al. 2018).

3.2 The mass $-$ metallicity plane

3.2.1 Fundamental properties and metallicity

The correlations between the gas-phase metallicity of a galaxy and its fundamental properties are expected to go beyond a simple power-law correlation between stellar mass and metallicity. Both in the local Universe and at high-redshifts, studies have suggested the existence of a fundamental plane connecting gas-phase metallicity, stellar mass and star-formation rate. Galaxies of higher star-formation rates are predicted to have lower metallicities at a given stellar mass, due to star-formation-driven winds and supernovae re-

moving metal-enriched gas from the inter-stellar medium as well as the dilution by metal-poor gas accretion (e.g. Ellison et al. 2008; Mannucci et al. 2010; Stott et al. 2013; Cresci et al. 2019; Curti et al. 2020a).

In Figure 3, we colour the galaxies by their dust-corrected Hα star-formation rate as a first route to identify this plane in our sample. The Hα dust correction is derived from SED fitting, (see Section 2). The indication of a weak correlation is clear, with more highly star-forming galaxies being below the median trend between stellar mass and gas-phase metallicity. To more solidly establish the presence of the fundamental plane, we measure each galaxy's offset to the median stellar mass $-$ metallicity relation in Figure 3. To do this we define the quantity ΔZ, where $\Delta Z \equiv Z_{\text{gal}} - Z_{\text{med}}$. Z_{gal} is the gas-phase metallicity of the galaxy whilst Z_{med} is the gas-phase metallicity given by an interpolation of the median track at the same stellar mass as the galaxy, shown in Figure 3. We use the median mass $-$ metallicity relation for each redshift subsample sample to measure ΔZ for all 644 galaxies in the observational sample.

In Figure 4, we show ΔZ as a function of the Hα derived star-formation rate, stellar continuum half-light radius (R_{h}), Hα specific star-formation rate (sSFR[yr^{-1}] $\equiv$ SFR$_{\text{H}\alpha}/M_*$) and the balance between Hα rotational velocity and velocity dispersion ($v_{\text{rot,H}\alpha}/\sigma_{\text{H}\alpha}$)[1]. We identify a strong correlation between ΔZ and star-formation rate, with a Spearman coefficient of $r = -0.79$ and the probability the correlation is due to chance $p = 0.002$. The linear parametric fit has a slope of -0.08 ± 0.03 (i.e. $2.6 - \sigma$ from being flat), whereby more highly star-forming galaxies have lower gas-phase metallicities for a given stellar mass. A similar trend is

---

[1] The rotation velocity and velocity dispersion for each galaxy are measured at $2R_{\text{h}}$ from the galaxy's spatially-resolved Hα kinematics. See Tiley et al. in prep. for details.
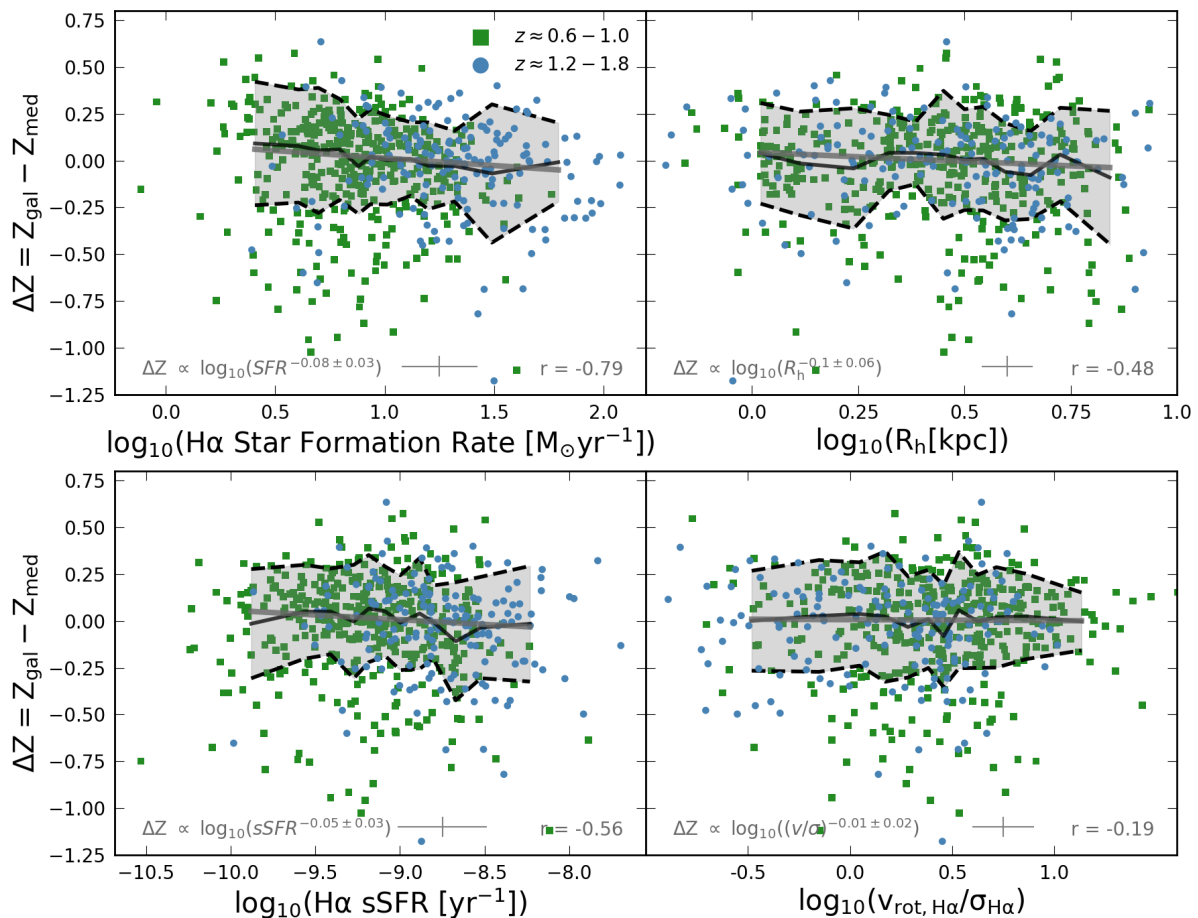
Figure 4. Offset from the median mass − metallicity relation (ΔZ) as a function of Hα star-formation rate (top-left panel), stellar continuum half-light radii ($R_{\rm h}$) (top-right panel), Hα specific star-formation rate (bottom-left panel) and $v_{\rm rot,H\alpha}/\sigma_{\rm H\alpha}$ (top-right panel) for galaxies at $z \approx 0.6 − 1.0$ and $z \approx 1.2 − 1.8$. The median mass − metallicity relation is derived by interpolating the running median shown in Figure 3. The grey shaded region and black dashed lines indicate the $1 − \sigma$ scatter region on the running median (black solid line) and in each panel. The grey line indicates a parametric fit to the running median, with parameters reported in the lower left corner of each panel. We also report the Spearman rank coefficient (r) of each correlation in the bottom-right corner of each panel. The median uncertainty is shown in the lower part of each panel. We identify a strong negative correlation between a galaxy's offset from the median mass − metallicity relation and its Hα star-formation rate ($r = -0.79$) and a moderate correlation with the galaxy's specific star formation ($r = -0.56$). We find a moderate correlation between the offset from the median mass − metallicity relation and the stellar continuum half-light radius ($r = -0.48$) whilst the ratio of rotational velocity and velocity dispersion shows no correlation with a galaxies position in the mass − metallicity plane. This indicates that more highly star-forming, larger galaxies have a lower metallicity at a fixed stellar mass irrespective of their rotation dominance.

identified individually in the $z \approx 0.6 − 1.0$ and $z \approx 1.2 − 1.8$ samples. To understand whether this correlation is driven by incompleteness at low star-formation rates and low metallicity, we exclude galaxies with $\log_{10}({\rm SFR}[{\rm M}_\odot\,{\rm yr}^{-1}]) < 0.5$ and re-fit the data. We again find a strong negative correlation with $r = -0.81$ ($p = 0.002$) at a $4.3 − \sigma$ level. We also fit to galaxies with $\log_{10}(M_*) < 10.0$, to understand the impact of incompleteness at high stellar masses due to the removal of AGN. We find a weaker trend with $r = -0.54$ ($p = 0.26$) at a $1.2 − \sigma$ level, indicating this a potential driver of the correlation.

This is in agreement with other studies of gas-phase metallicity in star-forming galaxies at high redshift (e.g. Mannucci et al. 2010; Stott et al. 2013; Zahid et al. 2014; Magdis et al. 2016; Sanders et al. 2018; Cresci et al. 2019). The dependence on star-formation rate is expected to be driven by gas accretion and cold gas inflows, especially at high redshift, that leads to an increase in the star-formation rate and a dilution of the interstellar medium's metal content.

As well as the ongoing star-formation rate of a galaxy correlating with the gas-phase metallicity, the specific star formation rate

(sSFR) has been suggested to weakly anti-correlate with metallicity (e.g. Ellison et al. 2008; Mannucci et al. 2010; Pilyugin et al. 2013; Sanders et al. 2018; Huang et al. 2019). For galaxies with $\log_{10}({\rm sSFR}[{\rm yr}^{-1}]) \geq -9.5$, at a given stellar mass, higher specific star formation systems are predicted to have lower gas-phase metallicity, whilst galaxies with $\log_{10}({\rm sSFR}[{\rm yr}^{-1}]) < -9.5$ have been shown to exhibit no significant correlation between sSFR and metallicity (e.g. Mannucci et al. 2010; Salim et al. 2015; Torrey et al. 2018). For our sample, we identify a moderate correlation between Hα derived specific star-formation rate and ΔZ with $r = -0.56$ ($p = 0.05$) corresponding to a $1.6 − \sigma$ significance which is in agreement with the anti-correlation identified by Magdis et al. (2016) between metallicity and specific star-formation rate main sequence offset (ΔsSFR) in the KROSS survey and also the 3-σ negative correlation identified by Sanders et al. (2018) between gas-phase metallicity and specific star-formation rate in the MOSDEF survey of 260 star-forming galaxies at $z \approx 2.3$. Fitting to galaxies with $\log_{10}({\rm sSFR}[{\rm yr}^{-1}]) \geq -9.5$, we identify a correlation of $r = -0.75$ ($p = 0.01$) with a $2.5 − \sigma$ significance.
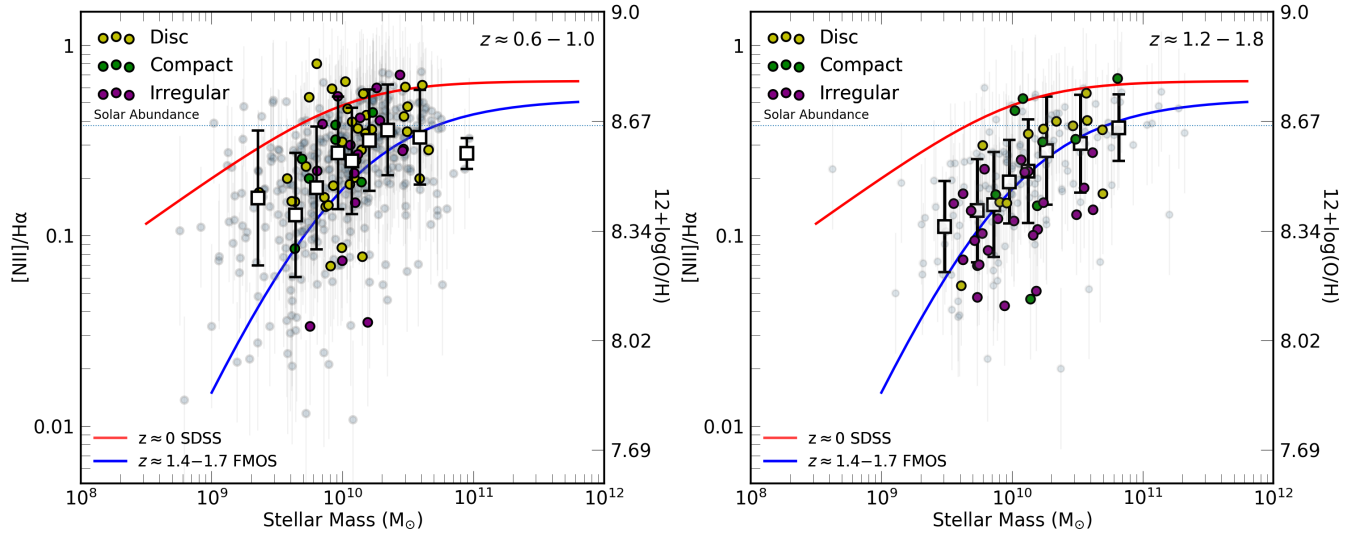
Figure 5. Mass−metallicity relation of the $z \approx 0.6-1.0$ (**left**) and $z \approx 1.2-1.8$ (**right**) samples with data points coloured according to the Huertas-Company et al. (2015) morphological classification of disc, compact or irregular. Galaxies without a classification are shown by the grey points. The red line represents the mass−metallicity relation at $z \approx 0$ derived from SDSS Survey (Curti et al. 2020a), whilst the blue line indicates the mass−metallicity relation at $z \approx 1.4-2.7$ from the FMOS survey (Zahid et al. 2014). The horizontal dotted line indicates solar metallicity (12+log(O/H) = 8.66; Asplund 2005). The metallicity is converted from a [NII]/Hα ratio to an Oxygen abundance following the calibration of Pettini & Pagel (2004). The white squares (and error bars) represent running medians and $1-\sigma$ scatters of the full sample. At $z \approx 0.6-1.0$ all morphological classes exhibit similar galaxy integrated gas-phase metallicity. At $z \approx 1.2-1.8$ irregular galaxies appear to have lower gas-phase metallicity than disc and spheroidal galaxies. Note the limit [NII]/Hα<0.8 at $z \approx 0.6-1.0$ and $z \approx 1.2-1.8$ to remove AGN, which are predominantly higher stellar mass galaxies.

Observational studies have also shown that the position of a galaxy in the mass−metallicity plane in the local Universe, and at high redshift, has a dependence on the physical extent of the galaxy (e.g. Ellison et al. 2008; Brisbin & Harwit 2012; Yabe et al. 2014; Huang et al. 2019). Galaxies with larger stellar continuum half-light radii, for a given stellar mass, exhibit lower gas-phase metallicity. This correlation was also found by Sánchez Almeida & Dalla Vecchia (2018) in the EAGLE hydrodynamical simulation, with smaller star-forming galaxies predicted to have higher metallicity from $z \approx 0-8$. To explore this correlation in our sample, in Figure 4 we also analyse the correlation between ΔZ and a galaxy's stellar continuum half-light radius.

We identify a moderate negative correlation at $1.6-\sigma$ between the continuum size of the galaxy and the offset from the median metallicity of the sample for a given stellar mass with a Spearman rank coefficient of $r = -0.48$ ($p = 0.12$). Only ≈ 60 per cent of the sample have stellar continuum half-light radii derived from *HST* imaging. If we exclude galaxies without *HST* imaging, whose continuum sizes are less certain, we identify a correlation between ΔZ and continuum size of similar significance with $r = -0.54$ ($p = 0.22$) at $2-\sigma$. This is in agreement with the correlation reported by other studies of star-forming galaxies (e.g. Ellison et al. 2008; Huang et al. 2019) and is attributed to smaller galaxies having higher stellar-mass surface densities and steeper potential wells, which are less effected by outflows and stellar winds removing metals from the interstellar medium.

Finally, in Figure 4 we also show the correlation between ΔZ and $v_{\rm rot,H\alpha}/\sigma_{H\alpha}$, identifying no correlation (Spearman rank coefficient of $r = -0.19$, $p = 0.55$). This indicates that more rotation-dominated galaxies have similar gas-phase metallicity to more dispersion-dominated galaxies at a given stellar mass. Zenocratti et al. (2020) showed that in the EAGLE simulation, more rotationally-supported galaxies at $z = 0$ with $\log_{10}(M_*) < 10.0$ have lower metallicities, whilst at higher stellar masses more dispersion-dominated

galaxies have lower metallicities. At higher redshift it was proposed that the correlation at lower stellar masses weakens whilst it is stronger for higher stellar-mass galaxies.

Refitting the correlation to just galaxies with $\log_{10}(M_*) > 10.0$, i.e. galaxies in which nuclear activity is more prevalent and mergers play a key role, the parametric fit has a slope of 0.03 ± 0.03 (i.e. consistent with no correlation) with a Spearman rank coefficient of $r = 0.43$ ($p = 0.33$). For galaxies with $\log_{10}(M_*) < 10.0$, i.e. galaxies in which star formation dominates the feedback, we find a moderate correlation with $r = 0.66$ ($p = 0.15$) and a parametric slope of 0.03 ± 0.02 (i.e. $1.5-\sigma$ significance). This is in contrast to the Zenocratti et al. (2020) results. It is well known that the rotation dominance of a galaxy is correlated with its morphology, with late-type disc galaxies exhibiting higher levels of rotation dominance, so next we explore the correlation between morphology and metallicity in our sample.

3.2.2 Morphology and metallicity

As well as the dynamical and photometric properties of a galaxy, a galaxy's morphology is known to correlate with its gas-phase metallicity (e.g Calura et al. 2009; Scudder et al. 2012; Grønnow et al. 2015; Horstman et al. 2020). In the local Universe galaxies with disturbed morphologies have been shown to have metallicities different than those of isolated galaxies, and that depends on the magnitude of the galaxy-galaxy interactions (e.g. Michel-Dansac et al. 2008; Rupke et al. 2010; Bustamante et al. 2018).

To explore this correlation within our sample, in Figure 5 we show the mass−metallicity relation for the two galaxy samples, according to the galaxy rest-frame optical morphology as classified by Huertas-Company et al. (2015). For $z \approx 0.6-1.0$ galaxies there is no variation of galaxy integrated gas-phase metallicity with morphological class. At $z \approx 1.2-1.8$ irregular galaxies have on average 0.11 ± 0.03 dex lower metallicities than the running median

of the sample at a given stellar mass, compared to spheroidal or disc galaxies that have on average 0.04 ± 0.03 and 0.06 ± 0.03 dex higher metallicities than the running median of the samples, respectively. To understand whether this trend is driven by sampling different regions of the galaxies between morphological classes, we also explore the correlation between the ratio of a galaxy's Hα extent to stellar extent (as parameterised by the stellar continuum half-light radius R_h) and morphological class, but we find no variation between spheroidal, disc and irregular galaxies.

In Gillman et al. (2019), irregular galaxies at $z \approx 1.2 - 1.8$ were inferred to have higher gas fractions in comparison to disc galaxies. A higher fraction of metal poor gas, potentially caused by inflows of low-metallicity gas due to the tidal forces and gravitational torques associated with previous galaxy interactions (e.g Bustamante et al. 2018), dilutes the metal content and leads to a lower observed metallicity at a given stellar mass, as shown in Figure 5. The irregular galaxies at $z \approx 1.2 - 1.8$ have a median stellar mass of $\log(M_*[M_\odot]) = 9.95$ whilst the disc and spheroidal galaxies have $\log(M_*[M_\odot]) = 10.28$ and $\log(M_*[M_\odot]) = 10.13$, respectively. The median Hα star-formation rate of the irregular galaxies at $z \approx 1.2 - 1.8$ is SFR$= 24 \pm 5$ M$_\odot$ yr^{-1} whilst disc and spheroidal galaxies have SFR$= 26 \pm 11$ and SFR$= 32 \pm 10$ M$_\odot$ yr^{-1} respectively.

Using the parameterisation of the fundamental plane between stellar mass, star-formation rate and gas-phase metallicity given by Curti et al. (2020a), we derive the expected metallicity of disc, spheroidal and irregular galaxies, if all three samples lie on the fundamental plane. The plane is parameterised as,

$$Z(M, SFR) = Z_0 - (\gamma/\beta)\log(1 + (M_*/M_0(SFR))^{-\beta}) \qquad (2)$$

where $\log(M_0(SFR)) = m_0 + m_1 \log(SFR)$. Curti et al. (2020a) established the best-fitting parameters are $Z_0 = 8.779 \pm 0.005$, $m_0 = 10.11 \pm 0.03$, $m_1 = 0.56 \pm 0.01$, $\gamma = 0.31 \pm 0.01$ and $\beta = 2.1 \pm 0.4$. Using Equation 2, we identify that disc and spheroidal galaxies at $z \approx 1.2 - 1.8$ have a median fundamental plane (FMR) metallicity of $Z_{\mathrm{disc,FMR}} = 8.59 \pm 0.02$ and $Z_{\mathrm{spheroidal,FMR}} = 8.52 \pm 0.01$, respectively. Irregular galaxies on the fundamental plane have a median metallicity of $Z_{\mathrm{irregular,FMR}} = 8.50 \pm 0.01$.

As we show in Figure 5, the disc and spheroidal galaxies of our sample at $z \approx 1.2 - 1.8$ have an actual median metallicity of $Z_{\mathrm{disc}} = 8.64 \pm 0.06$ and $Z_{\mathrm{spheroidal}} = 8.61 \pm 0.11$ respectively. Whilst irregular galaxies have a median metallicity of $Z_{\mathrm{irregular}} = 8.39 \pm 0.03$, in comparison to the solar abundance $Z_\odot = 8.66$ measured by Asplund (2005). This indicates that the irregular galaxies identified in our $z \approx 1.2 - 1.8$ sample do not lie on the fundamental mass − metallicity relation established by Curti et al. (2020a), in contrast to disc and spheroidal galaxies, that do lie on or near the plane. A similar result was also obtained by Bustamante et al. (2020) in the SDSS survey at $z \approx 0$. Bustamante et al. (2020) demonstrated that galaxies showing signs of interactions lie off the fundamental plane, exhibiting lower gas-phase metallicities. They concluded that the offset from the fundamental plane is driven by the recent triggering of gas inflows, that are stronger than those normally experienced by the 'main-sequence' star-forming galaxies that the fundamental plane describes.

4 METALLICITY GRADIENTS

Constraining the distribution of gas-phase metallicity in a galaxy provides insights into the baryonic processes (e.g. star formation,

feedback and accretion) that dominate a galaxy's evolution, and ultimately lead to changes in galaxy dynamics and morphology. Utilizing the spatially-resolved dynamics of the galaxies in our sample, we can analyse how a galaxy's gas-phase metallicity is correlated with radius and how this is connected to other galaxy properties such as those presented in Figure 4 (e.g. Hα star-formation rate and stellar continuum size).

In this section we analyse the [N$\textsc{ii}$]/Hα line ratio (i.e metallicity) gradients in our galaxies, including modelling of the systematics encountered in our analysis and consistency tests, in addition to correlating the metallicity gradients of the observational sample with the morphological and dynamical properties of the galaxies.
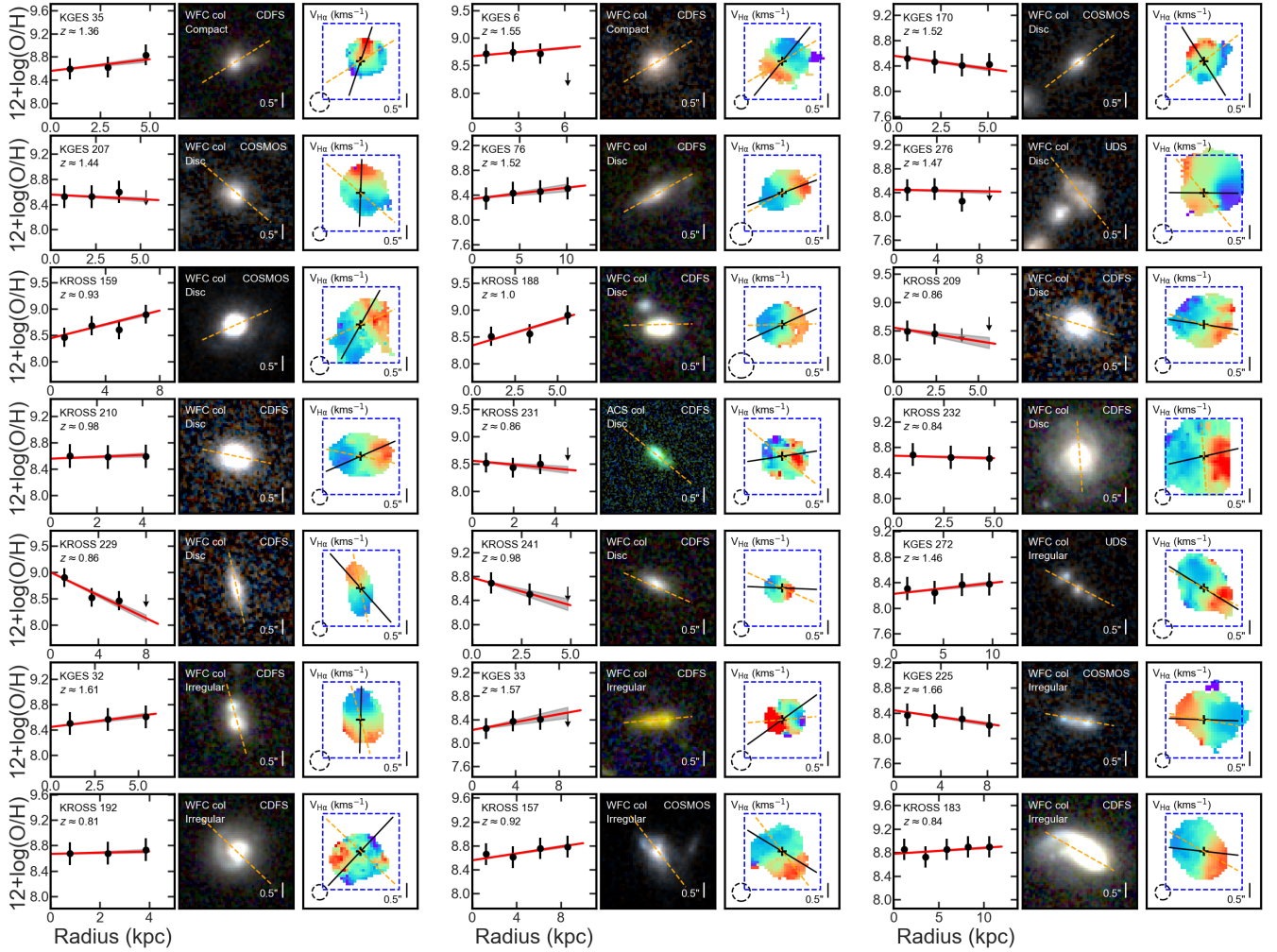
4.1 Radial metallicity profiles

To measure the radial dependence of the gas-phase metallicity of each, we sum the spectra in the de-redshifted data cube in elliptical annuli whose semi-major axes are multiples of the half-light radius of the PSF of the integral field data. The axis ratio, position angle and half-light radius of the galaxy are derived from *HST* CANDELS images (see Gillman et al. 2019). We fit a three Gaussian profiles to the Hα and [N$\textsc{ii}$] emission lines in each annulus as before, from which we measure the [N$\textsc{ii}$]/Hα ratio. To fit the emission lines we require the integrated Hα line of the annulus to have a signal-to-noise (S/N) ≥ 3. We extract the [N$\textsc{ii}$]/Hα ratio in all annuli where these criteria are met. If the [N$\textsc{ii}$] emission line has a S/N ≤ 3 we instead calculate a $3 - \sigma$ upper limit for [N$\textsc{ii}$]/Hα ratio (see Figure A1 for examples).

The emission lines are fit using the same χ^2 minimisation procedure as for the integrated spectra, with the FWHM and wavelength separation of the two [N$\textsc{ii}$] lines and Hα line fixed. Examples of the [N$\textsc{ii}$]/Hα ratio measurements for a number of galaxies are shown in Appendix A. If we have more than three measurements of [N$\textsc{ii}$]/Hα as a function of radius with at least one measurement not being a limit, we additionally measure the slope of the [N$\textsc{ii}$]/Hα ratio as a function of radius.

4.2 Consistencies and calibrations

Since our observations are ground-based and are sensitive to variations in galaxy properties (such as galaxy size or inclination) as well as seeing (see Section 4.3), it is important to quantify the reliability of our method to derive the intrinsic metallicity gradient of a galaxy. To test the reliability of the derived metallicity gradient, we analyse the effects of extracting the spectra in annuli with different position angles (e.g. PA$_{\mathrm{kin}}$, PA$_{\mathrm{morph}}$) and with varying semi-major axes (e.g. 2 kpc, $0.5R_h$, $R_{\mathrm{h,psf}}$). The results are presented in Gillman (2020), where we compared the metallicity gradients derived with different position angles and semi-major axes. We also explore the correlation between metallicity gradient and the axis ratio of the galaxy, identifying no correlation.

We demonstrated in Gillman (2020) that the choice of position angle and annulus size has no systematic impact on the measured [N$\textsc{ii}$]/Hα metallicity gradients. We thus conclude that our method of using annulus sizes relative to the size of the PSF of the integral field data, aligned with the galaxy's kinematic position angle, and adopting $3 - \sigma$ upper limits for low signal-to-noise regions to measure the metallicity gradients is robust and does not bias the measured gradients and uncertainties.

Figure 6. Examples of spatially-resolved compact, disc and irregular galaxies with measured [NII]/Hα gradients. For each galaxy, we show in the left panel the radial metallicity profile (black data points) and linear parametric fit (red solid line) with $1 - \sigma$ error (grey shaded region), and list the galaxy name and the Hα-derived $z_{\rm spec}$ in the top-left corner. A HST colour image with the morphological position angle overlaid (orange dashed line) is shown in the central panel, where we also list the HST instrument used, galaxy type and extragalactic deep field. Finally, we show in the right panel, the Hα velocity map with kinematic position angle (black solid line), kinematic centre (black cross), the FWHM of the seeing (black dashed circle) and KMOS IFU field of view (blue dashed square) overlaid. There is no correlation between the metallicity gradients of the galaxies and their rest-frame optical morphologies classified from the HST images.

4.3 Beam smearing

One of the most significant systematic effects that affects our ability to accurately measure the metallicity gradients of high-redshift galaxies is beam smearing (e.g. Yuan et al. 2013; Mast et al. 2014; Carton et al. 2017; Acharyya et al. 2020). The atmospheric seeing blurs the observed emission of each galaxy. The metallicity gradient measured is thus expected to be artificially flattened compared to the intrinsic gradient of the galaxy.

To quantify this effect and understand the impact on our measurements we generate 1000 mock galaxies with a given intrinsic metallicity gradient ranging from -0.07 to 0.07 dex kpc^{-1}. We then build mock datacubes with the same properties as our KMOS observations, convolve each velocity slice with the PSF and measure the observed metallicity gradient of the galaxy.

For these simulations, we model the Hα spatial distribution of the galaxies using two dimensional Sérsic profiles with an index of $n = 1$ (exponential disc) and a range of half-light radii, ellipticity and position angles that match the distribution of these observables in

the $z \approx 1.2 - 1.8$ and $z \approx 0.6 - 1.0$ samples. We assume the Hα half-light radius is equal to the stellar continuum half-light radius of each galaxy, and use this to define the annulus sizes from which we extract the [NII]/Hα ratios. To model the PSFs of the observations we use a circular two-dimensional Gaussian function, that is scaled relative to the size of the model galaxy. The velocity profiles of the input emission lines are a combination of Gaussian profiles and Gaussian noise, scaled to match the required signal-to-noise.

The results of the beam smearing modelling analysis is discussed in Appendix B. We derive a beam-smearing correction factor that is a function of FWHM/$R_{\rm h}$ and the axis ratio. We note we do not account for a dependence on the intrinsic metallicity gradient of the galaxy. As expected, galaxies with a larger FWHM/$R_{\rm h}$ ratio i.e a smaller stellar continuum half-light radius ($R_{\rm h}$) at fixed PSF FWHM, are more affected by beam-smearing. In addition at fixed FWHM/$R_{\rm h}$, more edge-on galaxies also have a larger correction factor. To correct the metallicity gradients measured in our observational sample for beam smearing, we interpolate the observed-

to-intrinsic gradient ratios as a function of FWHM/R_h for a given axis ratios as shown in Appendix B. We use the resulting correction curve to derive the beam smearing correction factor of each galaxy in our sample. The median beam smearing correction factor for the $z \approx 0.6-1.0$ sample is $C_{BS} = 0.66 \pm 0.17$ whilst for the $z \approx 1.2-1.8$ galaxies we derive a median factor of $C_{BS} = 0.64 \pm 0.18$.

For galaxies with FWHM/R_h ratios above ≈ 1, the observed metallicity gradient is <50 per cent of the intrinsic metallicity gradient and is therefore very uncertain. For the remainder of our analysis, we thus limit the sample and present the beam smearing-corrected metallicity gradients only in galaxies with a correction factor <50 per cent (98 galaxies). This sub-sample of galaxies has a distribution of stellar mass similar to that of the full observational sample whilst exhibiting larger stellar continuum sizes (see Appendix B). We note sub-sample shows a weak negative correlation between metallicity gradient and axis ratio that is not present in the full sample. This is due to incompleteness at low axis ratio values, as these galaxies have significant beam smearing correction factors.

The median beam smearing-corrected metallicity gradient, for the sample of 98 galaxies with robust beam smearing-corrected metallicity gradients, is $\Delta Z/\Delta R = 0.002 \pm 0.004$ dex kpc^{-1} (i.e. consistent with no gradient) with a $16-84$th percentile range of $\Delta Z/\Delta R = -0.034 - 0.043$ dex kpc^{-1}. We now explore the correlations between the galaxies beam smearing-corrected metallicity gradients and their morphological and dynamical properties.

4.4 Metallicity gradients and morphology

In the local Universe studies of the metallicity gradients in star-forming galaxies have established a link between galaxy morphology and the slope of the radial metallicity profile. Interacting galaxies have been shown to exhibit flattened gradients (e.g. Kewley et al. 2010; Rupke et al. 2010; Taylor & Kobayashi 2017), which is anticipated from inflows of low-metallicity gas into the galaxy centres as a result of the interactions. At high redshift integral-field studies of star-forming galaxies with irregular morphologies have revealed them to have inverted (positive) metallicity gradients, i.e metallicity increasing with radius (Queyrel et al. 2012).

Early- and late-type galaxies locally have been shown to exhibit a range of radial metallicity gradients, with some studies identifying no morphological dependence (e.g. Zaritsky et al. 1994; Sánchez et al. 2014; Sánchez-Menguiano et al. 2016) whilst others indicate that early-type galaxies have no gradient but late-type galaxies have seep (negative) abundance profiles (e.g. Márquez et al. 2002).

In Figure 6 we show examples of the kinematics and metallicity gradients of galaxies in our sample with *HST* imaging, for a range of rest-frame optical morphologies as determined by Huertas-Company et al. (2015). There is no correlation between the rest-frame optical morphologies of the galaxies, as indicated by the *HST* images, and the gradients of the metallicity profiles, with disc, spheroidal and irregular galaxies having a range of metallicity gradients. To search for a potential link between the gas-phase metallicity gradient and the rest-frame optical morphology of a galaxy, in Table 1 we show the median beam smearing-corrected gas-phase metallicity gradients of spheroidal, disc and irregular galaxies at $z \approx 0.6-1.0$ and $z \approx 1.2-1.8$. At $z \approx 0.6-1.0$ there are no spheroidal (compact) galaxies and at $z \approx 1.2-1.8$ there is only one spheroidal galaxy with a beam smearing correction factor less than 50 per cent. There is no difference between the metallicity gradients of the three morphological classes, with all galaxies having a median metallicity gradient within $1-\sigma$ of each other, even though their integrated gas-phase metallicities are different at $z \approx 1.2-1.8$ (Figure 5).

Table 1. Median beam smearing-corrected gas-phase metallicity gradients in spheroidal, disc and irregular galaxies at $z \approx 0.6-1.0$ and $z \approx 1.2-1.8$.

| Morphology	$\Delta Z/\Delta R$ [dex kpc^{-1}]	
	$z \approx 0.6-1.0$	$z \approx 1.2-1.8$
Compact	–	0.037 ± 0.004
Disc	-0.003 ± 0.010	0.005 ± 0.011
Irregular	0.011 ± 0.023	-0.006 ± 0.017

Recent studies of high-redshift star-forming galaxies have also established there is no correlation between a galaxy's metallicity gradient and its morphology. Curti et al. (2020b) identified no difference between the metallicity gradients of interacting and disturbed galaxies compared to non-interacting systems in a sample of 42 lensed galaxies at $z \approx 1.2-2.5$. They attributed this to the limited spatial resolution of their high-redshift data as well as the method of averaging the metallicity in annuli and thus smoothing out azimuthal variations of metallicity. High-resolution studies of local star-forming galaxies have also demonstrated the importance of resolving individual H II regions and azimuthal variations when analysing the connection between morphology and metallicity profiles (e.g. Sánchez et al. 2017a; Sánchez-Menguiano et al. 2018).

4.5 Metallicity gradients and fundamental properties

At low redshifts strong trends between the stellar masses, specific star-formation rates and metallicity gradients of star-forming galaxies have been observed (e.g. Sánchez et al. 2014; Belfiore et al. 2017, 2019). Less massive, high specific star-formation rate systems exhibit flatter metallicity gradients, whilst more massive, low specific star-formation rate galaxies have steeper (more negative) abundance gradients.

To analyse whether the metallicity gradients of the galaxies in our sample are correlated to other observable properties besides morphology, in Figure 7 we plot their metallicity gradients as a function of stellar mass, dust-corrected Hα derived star-formation rate and Hα specific star-formation rate. The stellar masses of the galaxies show a strong negative correlation with the metallicity gradients, with a Spearman rank coefficient of $r = -1.0$ ($p = 0$) and a slope of -0.03 ± 0.005 ($5-\sigma$ from flat). This indicates that higher stellar mass galaxies in our sample have steeper (more negative) metallicity gradients. The Hα star-formation rates indicates a no trend with the metallicity gradients with $r = 0.3$ ($p = 0.62$) and a non-zero slope at a $0.2-\sigma$ significance. The specific star-formation rate of the galaxies shows a moderate positive trend with $r = 0.80$ ($p = 0.1$) and a non-zero slope at a $2-\sigma$ level. Galaxies with a lower specific star-formation rates in our sample have steeper (more negative) metallicity gradients.

The correlation between specific star formation rates and radial metallicity gradients was also identified by other studies of high-redshift star-forming galaxies (e.g. Stott et al. 2014; Wuyts et al. 2016; Curti et al. 2020b), whereby galaxies with higher specific star-formation rates have metal-poorer centres. Hydrodynamical simulations have highlighted the importance of feedback in driving this correlation and shaping the metal distribution within galaxies (e.g. Ma et al. 2017), suggesting that in these lower stellar mass, higher specific star-formation rate galaxies, feedback is more efficient. The negative correlation between metallicity gradient and stellar mass is also consistent with with the inside-out model of galaxy evolution (e.g. Davé et al. 2011; Gibson et al. 2013), whereby the inner
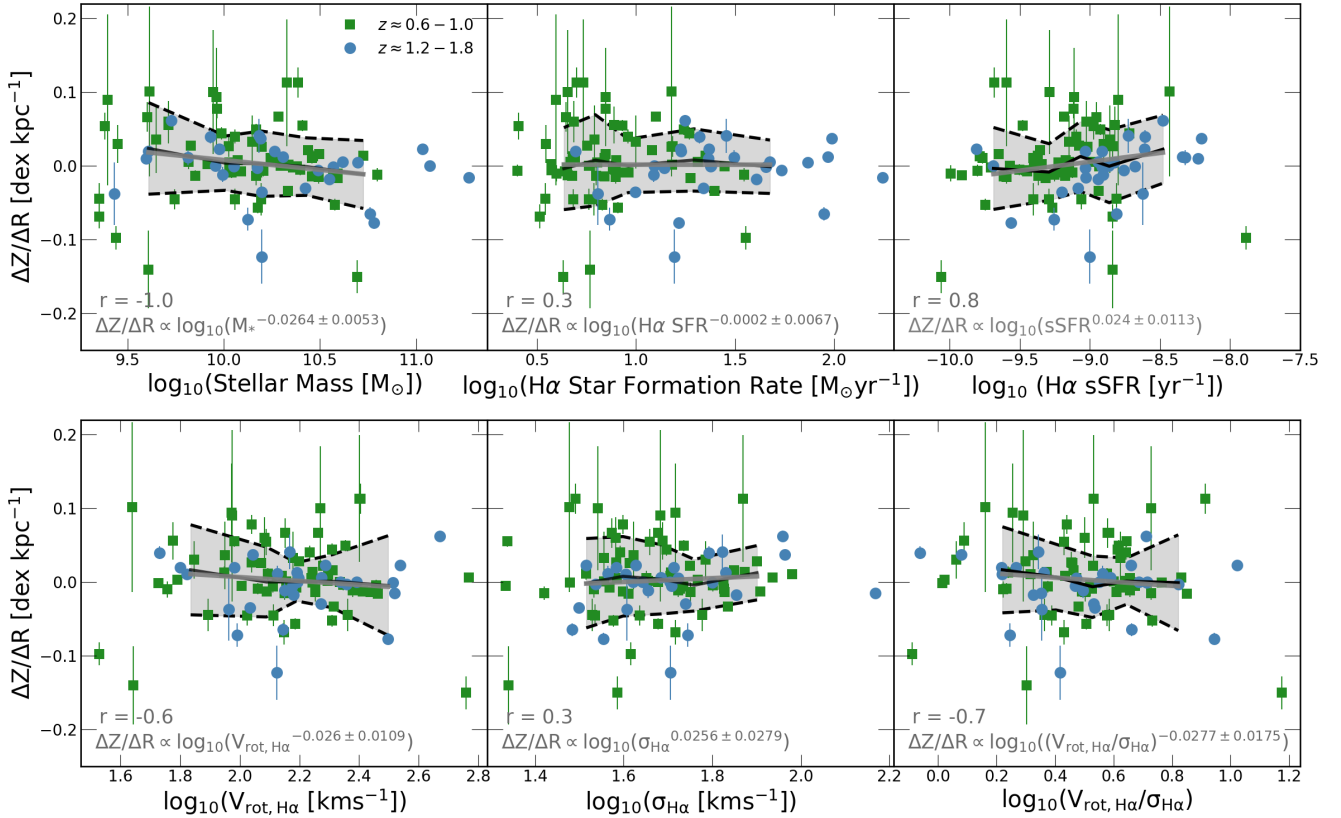
Figure 7. Bean smearing-corrected metallicity gradients of the galaxies our sample as a function of their stellar masses, dust-corrected Hα derived star-formation rates, Hα specific star-formation rates, rotational velocities, velocity dispersions and ratio of rotational velocity to velocity dispersion. The black dashed lines and grey-shaded regions indicate the $1 - \sigma$ scatters of the running medians (black solid lines). We also show a linear parametric fit to the running median of each relation, as shown in the lower-left corner of each panel and quantified by the Spearman rank coefficient. We identify a strong negative correlation with the stellar masses and a moderate positive correlation with specific star-formation rates but no significant correlation with the star-formation rates of the galaxies. The metallicity gradients of the galaxies show an insignificant positive correlation with the velocity dispersions, but a moderate positive (negative) correlation with the rotational velocities (rotation dominance, $v_{\mathrm{rot,H}\alpha}/\sigma_{\mathrm{H}\alpha}$).

regions of galaxies form stars at earlier times, leading to an increase in the metallicity in the central regions as the galaxies evolves.

Models of inside-out galaxy evolution also predict inflows of low-metallicity gas into the central regions of galaxies at early times, along filaments, that dilute the local metal distributions and boost the specific star-formation rate in the central regions. This may well be reflected in the tentative correlation seen in Figure 7 between the metallicity gradients and Hα specific star-formation rates of the galaxies in our sample.

Figure 7 also shows the correlation between the metallicity gradients of galaxies in the observed sample and their rotation velocities, velocity dispersions and the ratio of rotation velocity and velocity dispersion. We establish a moderate $2.3 - \sigma$ correlation between the metallicity gradient of a galaxy and its rotation velocity with a correlation coefficient of $r = -0.60$ ($p = 0.28$). Whilst we find no correlation with the velocity dispersion ($r = 0.30$, $p = 0.62$).

In the local Universe, studies of late-type galaxies in the MaNGA survey (e.g. Pilyugin et al. 2019) have shown that the metallicity gradients flatten with increasing rotation velocity, in contrast to our trend in Figure 7. Similarly Queyrel et al. (2012) established that, for star-forming galaxies at $z \approx 1.2$ in the Mass Assembly Survey with SINFONI in VVDS (MASSIV), galaxies with higher gas velocity dispersions have shallower or more positive metallicity gradients in agreement with Figure 7. We however identify a moderate negative correlation between the ratio of rota-

tion velocity to velocity dispersion ($v_{\mathrm{rot,H}\alpha}/\sigma_{\mathrm{H}\alpha}$) of a galaxy and its metallicity gradient, with $r = -0.70$ ($p = 0.18$) and a non-zero slope at a $1.6 - \sigma$ level.

Other studies of high-redshift galaxies have also identified that more dispersion dominated galaxies have flatter metallicity gradients (e.g. Jones et al. 2013; Leethochawalit et al. 2016; Ma et al. 2017; Hemler et al. 2020). It is expected that this correlation is driven by metal-rich gas being more effectively redistributed in dispersion dominated galaxies, thus flattening the metallicity gradients.

4.6 Cosmic evolution of metallicity gradients

Finally we compare the metallicity gradients of the galaxies in our sample to other observational studies of the chemical abundance gradients of star-forming galaxies across cosmic time. We also compare our results to cosmological hydrodynamical simulations which trace the gas-phase metallicities of disc galaxies from $z \approx 2$ to the present day.

In Figure 8 we show the metallicity gradients derived by Rupke et al. (2010) at $z \approx 0$ for a sample of isolated spiral galaxies as well as galaxies undergoing interactions with other systems. The interacting systems have slightly flatter gradients, with, $\langle \Delta Z/\Delta R \rangle = 0.02 \pm 0.05$ dex kpc^{-1} in comparison to isolated systems with $\langle \Delta Z/\Delta R \rangle = -0.04 \pm 0.05$ dex kpc^{-1}.

At intermediate redshift we use the distribution of metallicity
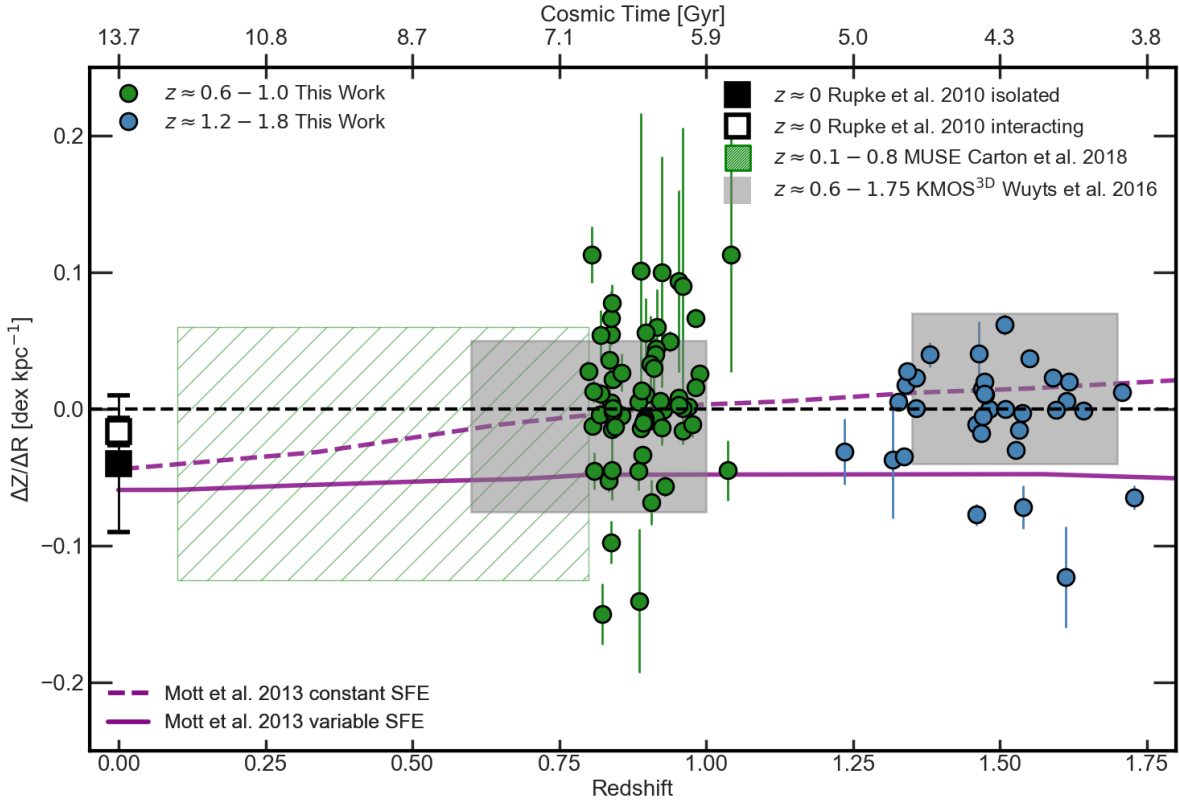
Figure 8. Beam smearing-corrected metallicity gradients of the galaxies in our sample as a function of their redshifts. We also show the metallicity gradients of a $z \approx 0$ sample of isolated and interacting star-forming galaxies from Rupke et al. (2010) (respectively black and white square with error bars). The green hashed region indicates measurements from MUSE observations of intermediate-redshift galaxies from Carton et al. (2018). The metallicity gradients derived by Wuyts et al. (2016) from the KMOS^{3D} survey are indicated by the grey shaded regions. We also show theoretical predictions from two models of the metallicity gradients of disc galaxies from Mott et al. (2013) with radially constant star-formation efficiency (purple dashed line) and variable star formation efficiencies (solid purple line). The metallicity gradients measured from our sample are in agreement with other observations of star-forming galaxies at high redshifts as well as theoretical models. There is no significant evolution with redshift between the redshift samples with both samples exhibiting flatter gradients than observed locally.

gradients of star-forming galaxies from $z \approx 0.1 − 0.8$ derived by Carton et al. (2018) using Multi Unit Spectroscopic Explorer (MUSE) observations. These metallicity gradients are derived using a combination of strong forbidden lines and Balmer emissions lines. In Figure 8 we also show the [NII]/Hα metallicity gradients derived by Wuyts et al. (2016) for the KMOS^{3D} survey at $z \approx 0.6 − 1.8$, which are largely in agreement with those measured for our sample.

Finally, to compare to the predictions of hydrodynamical simulations, we show the tracks from Mott et al. (2013) who model the evolution of abundance gradients in spiral galaxies in the framework of inside-out disc formation. We show two models, one with variable star-formation efficiencies within galaxy discs, and one with a fixed star-formation efficiency that recreates the inverted gradients seen at high redshifts. Mott et al. (2013) note that the inversion of the gradients is predominantly driven by efficient feedback mechanisms and the infall of pristine gas, counteracting chemical enrichment, at early times.

Figure 8 indicates no significant evolution of the metallicity gradients with redshift between the $z \approx 0.6 − 1.0$ and $z \approx 1.2 − 1.8$ samples. At $z \approx 0.6 − 1.0$ the median metallicity gradient is $\Delta Z / \Delta R = −0.004 \pm 0.005$ dex kpc^{-1} with a $16 − 84$th percentile range of $−0.03 − 0.05$ dex kpc^{-1}. At $z \approx 1.2 − 1.8$ the median metallicity gradient is $\Delta Z / \Delta R = 0.0002 \pm 0.0048$ dex kpc^{-1} with a $16 − 84$th percentile range of $−0.03 − 0.02$ dex kpc^{-1}.

Our sample exhibits flatter metallicity gradients than those ob-

served locally but is consistent with previous studies of the metallicity gradients of high-redshift star–forming galaxies (e.g. Wuyts et al. 2016; Carton et al. 2018; Curti et al. 2020b). This flattening of metallicity gradients at earlier cosmic times (higher redshift) is also found in hydrodynamical simulations when strong feedback processes are implemented (e.g Mott et al. 2013; Tissera et al. 2019; Hemler et al. 2020).

The flattening of a galaxy's metallicity gradient could be caused by a number of processes. Galaxy interactions and mergers can lead to radial inflows of metal-poor gas, resulting in the dilution of the central metal abundance (e.g. Rupke et al. 2010). Feedback processes such star-formation-driven winds and supernovae, which are ubiquitous at high redshifts also act to reduce the metallicities of the central regions of star-forming galaxies in inside-out models of galaxy evolution (e.g. Newman et al. 2012; Swinbank et al. 2019; Förster Schreiber et al. 2019).

5 CONCLUSIONS

We have analysed the gas-phase metallicities of 644 typical star-forming galaxies at $z \approx 0.6 − 1.8$, utilising the [NII]/Hα emission line ratio as a probe. Using the spatially-resolved Hα kinematics and morphological properties of the galaxies we, analyse the connection between gas-phase metallicity, galaxy dynamics and morphology. We summarize our findings as follows:

• We establish that a gas-phase metallicity – stellar mass relation is present at $z \approx 0.8$ and $z \approx 1.5$ (Figure 3), with more massive galaxies exhibiting higher metallicity. We demonstrate that the $z \approx 0.6 - 1.0$ sample galaxies with a median stellar mass of $\log(M_*[M_\odot]) = 10.0$ has a median gas-phase metallicity of $12 + \log(O/H) = 8.56 \pm 0.01$. Whilst at $z \approx 1.2 - 1.8$, the galaxies in our sample with a median stellar mass of $\log(M_*[M_\odot]) = 10.0$ have a median gas-phase metallicity of $12 + \log(O/H) = 8.49 \pm 0.02$.

• At a fixed stellar mass, galaxies with higher Hα-derived star-formation rates (and specific star-formation rates) have lower gas-phase metallicity indicating the presence of a mass – metallicity – star-formation rate fundamental plane (Figure 4) with $\Delta Z \propto \log_{10}(SFR^{-0.08 \pm 0.03})$. We also identify that at fixed stellar mass, smaller galaxies (higher surface mass density) have higher gas-phase metallicities, with $\Delta Z \propto \log_{10}(R_h^{-0.1 \pm 0.06})$. We establish there is no dependence on the rotation dominance of the galaxy and its position in the mass – metallicity plane.

• Utilizing the morphological classifications of Huertas-Company et al. (2015), we determine that at $z \approx 0.6 - 1.0$ spheroidal, disc and irregular galaxies exhibit similar gas-phase metallicities whilst at $z \approx 1.2 - 1.8$, irregular galaxies have 0.11 ± 0.03 dex lower metallicities on average than disc and spheroidal galaxies, which are on average 0.04 ± 0.03 and 0.06 ± 0.03 dex above the median metallicity of the sample galaxies (Figure 5). We attribute these lower metallicities to the higher gas fractions found in irregular galaxies at $z \approx 1.5$ (Gillman et al. 2019).

• To quantify the metallicity gradients of our sample we measure the [NII]/Hα emission line ratio as a function of galactocentric radius using the spatially-resolved Hα data. We explore the correlation between metallicity gradient and other galaxy properties as well as the impact of beam smearing on our measurements of the metallicity gradient. For the sub-sample of 98 galaxies for which our simulations suggest a reliable intrinsic metallicity gradient can be inferred (median $\log(M_*[M_\odot]) = 10.16$ and SFR $= 8 \pm 1 M_\odot$ yr^{-1}), the median intrinsic metallicity gradient is $\Delta Z/\Delta R = 0.002 \pm 0.004$ dex kpc^{-1} with a $16 - 84$th percentile range of $\Delta Z/\Delta R = -0.034 - 0.043$ dex kpc^{-1}.

• Spheroidal, disc and irregular galaxies at $z \approx 0.61.8 -$ have gas-phase metallicity gradients similar to each other. However we establish a strong correlation ($r = -1.0$) at a $5 - \sigma$ level between the galaxies' stellar masses and metallicity gradients whereby more massive galaxies have steeper (more negative) abundance profiles (Figure 7). The rotation dominance (v/σ) is also identified to weakly correlate at a $1.6 - \sigma$ level ($r = -0.70$) with the metallicity gradients of our galaxies. More rotation-dominated galaxies have more negative metallicity gradients, as they are less efficient at redistributing metal-rich gas.

• Finally, we examine the metallicity gradients in the context of cosmic evolution (Figure 8). We demonstrate that our measurements of the metallicity gradients are consistent with flat gradients, that are reproduced in numerical simulations of high-redshift galaxies in which feedback plays a key role. We find no significant evolution between the two redshift samples with the $z \approx 0.6 - 1.0$ sample having a median metallicity gradient of $\Delta Z/\Delta R = -0.004 \pm 0.005$ dex kpc^{-1} with a $16 - 84$th percentile range of $-0.03 - 0.05$ dex kpc^{-1}. At $z \approx 1.2 - 1.8$ the median metallicity gradient is $\Delta Z/\Delta R = -0.0002 \pm 0.00048$ dex kpc^{-1} with a $16 - 84$th percentile range of $-0.03 - 0.02$ dex kpc^{-1}.

Overall we have shown that the gas-phase metallicity scaling relations of high-redshift star-forming galaxies are comparable to those in the local Universe, whilst being offset to lower metallicities.

We found no difference between the metallicity gradients of irregular and disc galaxies. This may well be due to the limited spatial resolution of our observations, and the azimuthal smoothing that occurs when deriving a metallicity gradient. Future observations with VLT/ERIS and ELT/HARMONI will allow ~kpc resolution observations of the interstellar medium of high-redshift galaxies, that will enable spatially-resolved scaling relations and metallicity gradients to be derived more accurately at high redshift.

DATA AVAILABILITY

The data underlying this article are available at http://astro.dur.ac.uk/KROSS/data.html for the $z \approx 0.6 - 1.0$ sample. The $z \approx 1.2 - 1.8$ sample data will be made available at http://astro.dur.ac.uk/kmos/kges/ upon the publication of Tiley et al. in prep.

REFERENCES

Acharyya A., Krumholz M. R., Federrath C., Kewley L. J., Goldbaum N. J., Sharp R., 2020, MNRAS, 495, 3819

Anglés-Alcázar D., Davé R., Özel F., Oppenheimer B. D., 2014, ApJ, 782, 84

Anglés-Alcázar D., Faucher-Giguère C.-A., Kereš D., Hopkins P. F., Quataert E., Murray N., 2017, MNRAS, 470, 4698

Arimoto N., Yoshii Y., 1987, A&A, 173, 23

Asplund M., 2005, ARA&A, 43, 481

Belfiore F., et al., 2017, MNRAS, 469, 151

Belfiore F., Vincenzo F., Maiolino R., Matteucci F., 2019, MNRAS, 487, 456

Boissier S., Prantzos N., 1999, MNRAS, 307, 857

Bolzonella M., Miralles J.-M., Pelló R., 2000, A&A, 363, 476

Brisbin D., Harwit M., 2012, ApJ, 750, 142

Brooks A. M., Governato F., Booth C. M., Willman B., Gardner J. P., Wadsley J., Stinson G., Quinn T., 2007, ApJ, 655, L17

Bundy K., et al., 2015, ApJ, 798, 7

Bustamante S., Sparre M., Springel V., Grand R. J. J., 2018, MNRAS, 479, 3381

Bustamante S., Ellison S. L., Patton D. R., Sparre M., 2020, MNRAS, 494, 3469

Calura F., Matteucci F., 2006, MNRAS, 369, 465

Calura F., Pipino A., Chiappini C., Matteucci F., Maiolino R., 2009, A&A, 504, 373

Calzetti D., Kinney A. L., Storchi-Bergmann T., 1994, ApJ, 429, 582

Carton D., et al., 2017, MNRAS, 468, 2140

Carton D., et al., 2018, MNRAS, 478, 4293

Chabrier G., 2003, PASP, 115, 763

Chisholm J., Tremonti C., Leitherer C., 2018, MNRAS, 481, 1690

Christensen C. R., Davé R., Brooks A., Quinn T., Shen S., 2018, ApJ, 867, 142

Collacchioni F., Lagos C. D. P., Mitchell P. D., Schaye J., Wisnioski E., Cora S. A., Correa C. A., 2020, MNRAS, 495, 2827

Cresci G., Mannucci F., Maiolino R., Marconi A., Gnerucci A., Magrini L., 2010, Nature, 467, 811

Cresci G., Mannucci F., Curti M., 2019, A&A, 627, A42

Curti M., Mannucci F., Cresci G., Maiolino R., 2020a, MNRAS, 491, 944

Curti M., et al., 2020b, MNRAS, 492, 821

Davé R., Finlator K., Oppenheimer B. D., 2011, MNRAS, 416, 1354

Davé R., Finlator K., Oppenheimer B. D., 2012, MNRAS, 421, 98

De Rossi M. E., Bower R. G., Font A. S., Schaye J., Theuns T., 2017, MNRAS, 472, 3354

Donley J. L., et al., 2012, ApJ, 748, 142

Ellison S. L., Patton D. R., Simard L., McConnachie A. W., 2008, ApJ, 672, L107

Erb D. K., 2008, ApJ, 674, 151

Erb D. K., Shapley A. E., Pettini M., Steidel C. C., Reddy N. A., Adelberger K. L., 2006, ApJ, 644, 813

Finlator K., 2017, Gas Accretion and Galactic Chemical Evolution: Theory and Observations. p. 221, doi:10.1007/978-3-319-52512-9_10

Förster Schreiber N. M., et al., 2018, ApJS, 238, 21

Förster Schreiber N. M., et al., 2019, ApJ, 875, 21

Gao Y., et al., 2018, ApJ, 868, 89

Garnett D. R., 2002, ApJ, 581, 1019

Giacconi R., et al., 2001, ApJ, 551, 624

Gibson B. K., Pilkington K., Brook C. B., Stinson G. S., Bailin J., 2013, A&A, 554, A47

Gillman S., 2020, PhD thesis, Durham University

Gillman S., et al., 2019, MNRAS, p. 3205

Grogin N. A., et al., 2011, ApJS, 197, 35

Grønnow A. E., Finlator K., Christensen L., 2015, MNRAS, 451, 4005

Harrison C. M., et al., 2017, MNRAS, 467, 1965

Hemler Z. S., et al., 2020, arXiv e-prints, p. arXiv:2007.10993

Hinshaw G., et al., 2013, ApJS, 208, 19

Horstman K., et al., 2020, arXiv e-prints, p. arXiv:2008.04327

Huang C., et al., 2019, ApJ, 886, 31

Huertas-Company M., et al., 2015, AJ, 809, 95

Jones T. A., Swinbank A. M., Ellis R. S., Richard J., Stark D. P., 2010, MNRAS, 404, 1247

Jones T., Ellis R. S., Richard J., Jullo E., 2013, ApJ, 765, 48

Kaplan K. F., et al., 2016, MNRAS, 462, 1642

Kennicutt Robert C. J., 1998, ApJ, 498, 541

Kewley L. J., Rupke D., Zahid H. J., Geller M. J., Barton E. J., 2010, ApJ, 721, L48

Köppen J., Edmunds M. G., 1999, MNRAS, 306, 317

Lawrence A., et al., 2007, MNRAS, 379, 1599

Leethochawalit N., Jones T. A., Ellis R. S., Stark D. P., Richard J., Zitrin A., Auger M., 2016, ApJ, 820, 84

Lequeux J., Peimbert M., Rayo J. F., Serrano A., Torres-Peimbert S., 1979, A&A, 500, 145

Lian J., Thomas D., Maraston C., Goddard D., Comparat J., Gonzalez-Perez V., Ventura P., 2018, MNRAS, 474, 1143

Lilly S. J., Cowie L. L., Gardner J. P., 1991, ApJ, 369, 79

Lilly S. J., Carollo C. M., Pipino A., Renzini A., Peng Y., 2013, ApJ, 772, 119

Lu Z., Mo H. J., Lu Y., 2015, MNRAS, 450, 606

Ma X., Hopkins P. F., Feldmann R., Torrey P., Faucher-Giguère C.-A., Kereš D., 2017, MNRAS, 466, 4780

Magdis G. E., et al., 2016, MNRAS, 456, 4533

Maiolino R., et al., 2008, A&A, 488, 463

Mannucci F., Cresci G., Maiolino R., Marconi A., Gnerucci A., 2010, MNRAS, 408, 2115

Mannucci F., Salvaterra R., Campisi M. A., 2011, MNRAS, 414, 1263

Márquez I., Masegosa J., Moles M., Varela J., Bettoni D., Galletta G., 2002, A&A, 393, 389

Mast D., et al., 2014, A&A, 561, A129

Michel-Dansac L., Lambas D. G., Alonso M. S., Tissera P., 2008, MNRAS, 386, L82

Mobasher B., et al., 2015, ApJ, 808, 101

Molina J., Ibar E., Swinbank A. M., Sobral D., Best P. N., Smail I., Escala A., Cirasuolo M., 2017, MNRAS, 466, 892

Mott A., Spitoni E., Matteucci F., 2013, MNRAS, 435, 2918

Newman S. F., et al., 2012, ApJ, 761, 43

Pettini M., Pagel B. E. J., 2004, MNRAS, 348, L59

Pilkington K., et al., 2012, A&A, 540, A56

Pilyugin L. S., Lara-López M. A., Grebel E. K., Kehrig C., Zinchenko I. A., López-Sánchez Á. R., Vílchez J. M., Mattsson L., 2013, MNRAS, 432, 1217

Pilyugin L. S., Grebel E. K., Zinchenko I. A., Nefedyev Y. A., Vílchez J. M., 2019, A&A, 623, A122

Poetrodjojo H., et al., 2018, MNRAS, 479, 5235

Queyrel J., et al., 2012, A&A, 539, A93

Rupke D. S. N., Kewley L. J., Chien L. H., 2010, ApJ, 723, 1255

Salim S., Lee J. C., Davé R., Dickinson M., 2015, ApJ, 808, 25

Sánchez Almeida J., Dalla Vecchia C., 2018, ApJ, 859, 109

Sánchez Almeida J., Sánchez-Menguiano L., 2019, ApJ, 878, L6

Sánchez-Menguiano L., et al., 2016, A&A, 587, A70

Sánchez-Menguiano L., et al., 2018, A&A, 609, A119

Sánchez-Menguiano L., Sánchez Almeida J., Muñoz-Tuñón C., Sánchez S. F., Filho M., Hwang H.-C., Drory N., 2019, ApJ, 882, 9

Sánchez S. F., et al., 2012, A&A, 538, A8

Sánchez S. F., et al., 2014, A&A, 563, A49

Sánchez S. F., Sánchez-Menguiano L., Pérez I., 2017a, in Cosmic Feast of the Elements. p. 35

Sánchez S. F., et al., 2017b, MNRAS, 469, 2121

Sanders R. L., et al., 2015, ApJ, 799, 138

Sanders R. L., et al., 2018, ApJ, 858, 99

Sanders R. L., et al., 2020, arXiv e-prints, p. arXiv:2009.07292

Scoville N., et al., 2007, ApJS, 172, 1

Scudder J. M., Ellison S. L., Torrey P., Patton D. R., Mendel J. T., 2012, MNRAS, 426, 549

Sharples R. M., et al., 2004, in Moorwood A. F. M., Iye M., eds, Proc. SPIEVol. 5492, Ground-based Instrumentation for Astronomy. pp 1179–1186, doi:10.1117/12.550495

Sharples R., et al., 2013, The Messenger, 151, 21

Sillero E., Tissera P. B., Lambas D. G., Michel-Dansac L., 2017, MNRAS, 472, 4404

Sobral D., Smail I., Best P. N., Geach J. E., Matsuda Y., Stott J. P., Cirasuolo M., Kurk J., 2013, MNRAS, 428, 1128

Sobral D., et al., 2015, MNRAS, 451, 2303

Somerville R. S., Davé R., 2015, ARA&A, 53, 51

Steidel C. C., Adelberger K. L., Dickinson M., Giavalisco M., Pettini M., Kellogg M., 1998, ApJ, 492, 428

Steidel C. C., Erb D. K., Shapley A. E., Pettini M., Reddy N., Bogosavljević M., Rudie G. C., Rakic O., 2010, ApJ, 717, 289

Stern D., et al., 2012, ApJ, 753, 30

Stott J. P., et al., 2013, MNRAS, 436, 1130

Stott J. P., et al., 2014, MNRAS, 443, 2695

Stott J. P., et al., 2016, MNRAS, 457, 1888

Swinbank A. M., Sobral D., Smail I., Geach J. E., Best P. N., McCarthy I. G., Crain R. A., Theuns T., 2012, MNRAS, 426, 935

Swinbank A. M., et al., 2019, MNRAS, 487, 381

Taylor P., Kobayashi C., 2017, MNRAS, 471, 3856

Tissera P. B., Rosas-Guevara Y., Bower R. G., Crain R. A., del P Lagos C., Schaller M., Schaye J., Theuns T., 2019, MNRAS, 482, 2208

Torrey P., et al., 2018, MNRAS, 477, L16

Tremonti C. A., et al., 2004, ApJ, 613, 898

Tumlinson J., et al., 2011, Science, 334, 948

Wang X., et al., 2017, ApJ, 837, 89

Wuyts S., et al., 2013, ApJ, 779, 135

Wuyts E., et al., 2016, ApJ, 827, 74

Yabe K., et al., 2014, MNRAS, 437, 3647

Yabe K., et al., 2015, PASJ, 67, 102

Yuan T. T., Kewley L. J., Rich J., 2013, ApJ, 767, 106

Zahid H. J., Kewley L. J., Bresolin F., 2011, ApJ, 730, 137

Zahid H. J., et al., 2014, ApJ, 792, 75

Zaritsky D., Kennicutt Robert C. J., Huchra J. P., 1994, ApJ, 420, 87

Zenocratti L. J., De Rossi M. E., Lara-López M. A., Theuns T., 2020, MNRAS,

van der Wel A., et al., 2014, ApJ, 788, 28

APPENDIX A: METALLICITY PROFILES
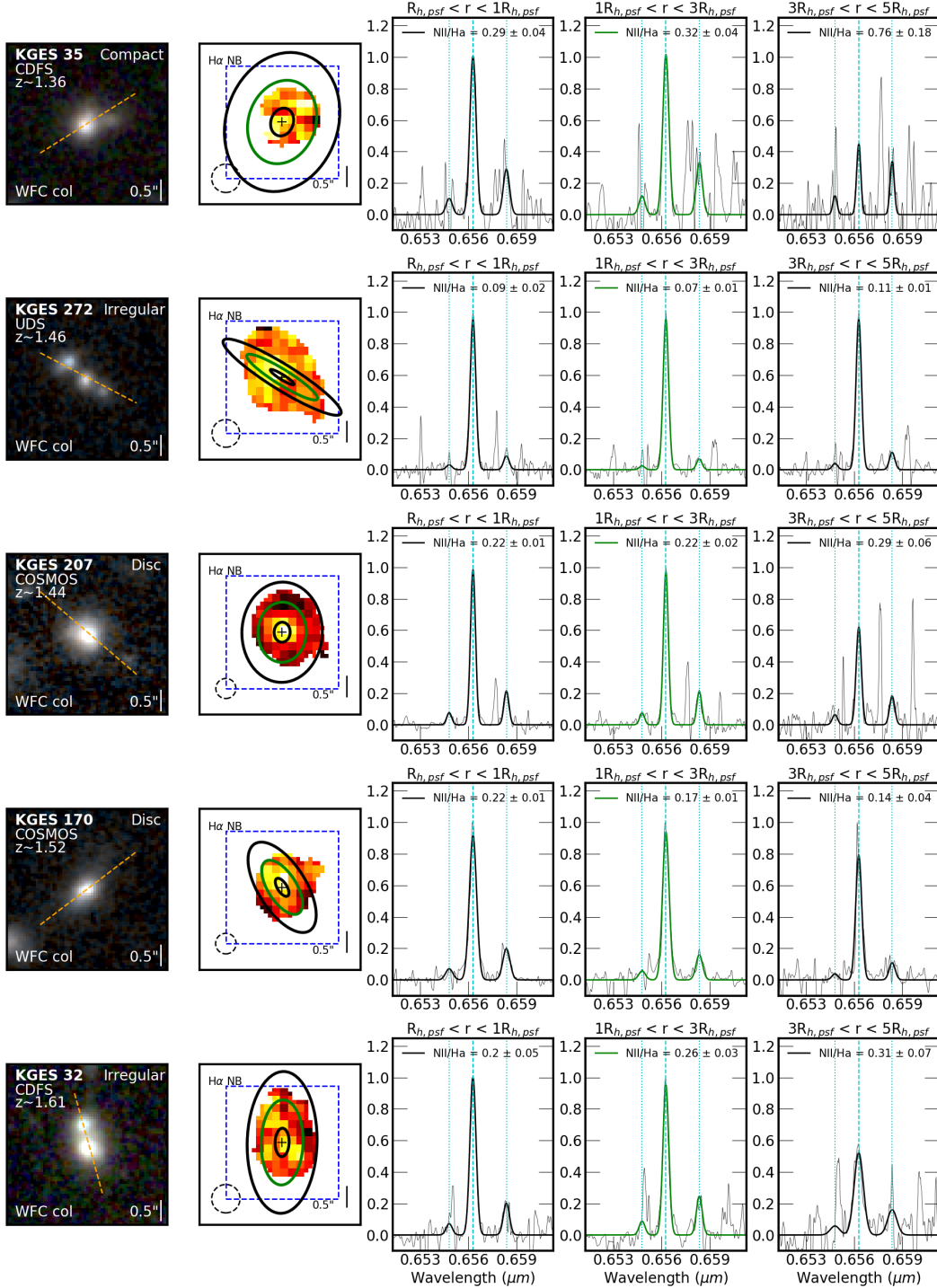
Figure A1. Examples of typical spatially-resolved galaxies, with from left to right, *HST* colour image with the semi-major axis indicated (orange line). Hα narrow band image from zero pointed observation, with KMOS field of view (blue dashed square) and annuli of multiples of $R_{h,psf}$ (HWHM of a Gaussian PSF) with galaxy's axis ratio and position equal to the kinematic position angle of the galaxy. Spectrum extracted from each annulus is shown with the Hα and [NII] Gaussian model overlaid. A range of [NII]/Hα profiles are shown with some galaxies displaying positive profiles increasing [NII]/Hα line ratio with radius and others negative.

APPENDIX B: BEAM SMEARING

In this section we derive beam smearing corrections for the metallicity gradients of the galaxies. As a first approach, to analyse the impact of axis ratio and beam smearing, we generate 1000 galaxies with infinite signal to noise. In Figure B1 we show the ratio of the recovered metallicity gradient to the intrinsic gradient as a function of the galaxies axis ratio and the ratio of the half-light radius to the FWHM of the PSF. We identify no correlation with the axis ratio of the galaxy, in our ability to recover the intrinsic metallicity gradient of the galaxy. The offset from unity in Figure B1, is caused by the finite sampling on the pixel grid of the continuous Sérsic distribution used to model the profile. The model galaxies have a median value of ($\Delta Z/\Delta R$ measured)/($\Delta Z/\Delta R$ intrinsic) = 0.98 ± 0.01. We correct for this finite sampling before modelling the impact of beam smearing on the metallicity gradients.

In Figure B1 we also show the ratio of the measured gradient to intrinsic gradient as a function of FWHM/R_h. For galaxies with a larger FWHM/R_h, the accuracy of the metallicity gradient measurement reduces significantly. We also identify an axis ratio dependence, with more edge on galaxies at a fixed FWHM/R_h requiring a larger correction than face-on galaxies. A similar trend was found by Stott et al. (2014). In more edge-on systems in the minor axis direction, the annuli are closer together, thus more affected by the spherical Gaussian PSF we use to model the turbulence in the atmosphere.

To understand the impact of signal to noise on our ability to measure the metallicity gradient, we generate a further 1000 galaxies with Hα signal to noise comparable to that of the observations. In Figure B2 we show the relations between the ratio of measured and intrinsic gradient as a function of axis ratio and FWHM/R_h. We identify the same correlations with FWHM/R_h in the lower signal to noise models but with more scatter. The median beam smearing correction for galaxies with Hα signal to noise comparable to the observations, across a range of FWHM/R_h, is ($\Delta Z/\Delta R$ |$_{measured}$) / ($\Delta Z/\Delta R$ |$_{intrinsic}$) = 0.45 ± 0.02, i.e. the observed gradient is 45 per cent of the intrinsic gradient.

At fixed axis ratio, we interpolate the observed gradient to intrinsic gradient ratio as a function of FWHM/R_h. We use this correction curve (and uncertainty) to derive beam smearing corrections for each galaxy in our sample. In Figure B2 we show a histogram of the observed and beam-smear correct intrinsic metallicity gradients of the sample. For a number of galaxies in our sample the beam smearing correction factor is larger than 50 per cent. A measurement of the intrinsic metallicity gradient of these galaxies is therefore very uncertain. We restrict our analysis of the metallicity gradients and their correlation with galaxy properties, to galaxies whose beam-smear correction factor is less than 50 per cent (98 galaxies). As shown in Figure B3, the sub-sample of 98 galaxies have a similar distribution of stellar mass to the full observational sample whilst exhibiting larger stellar continuum sizes by this selection.

This paper has been typeset from a TEX/LATEX file prepared by the author.
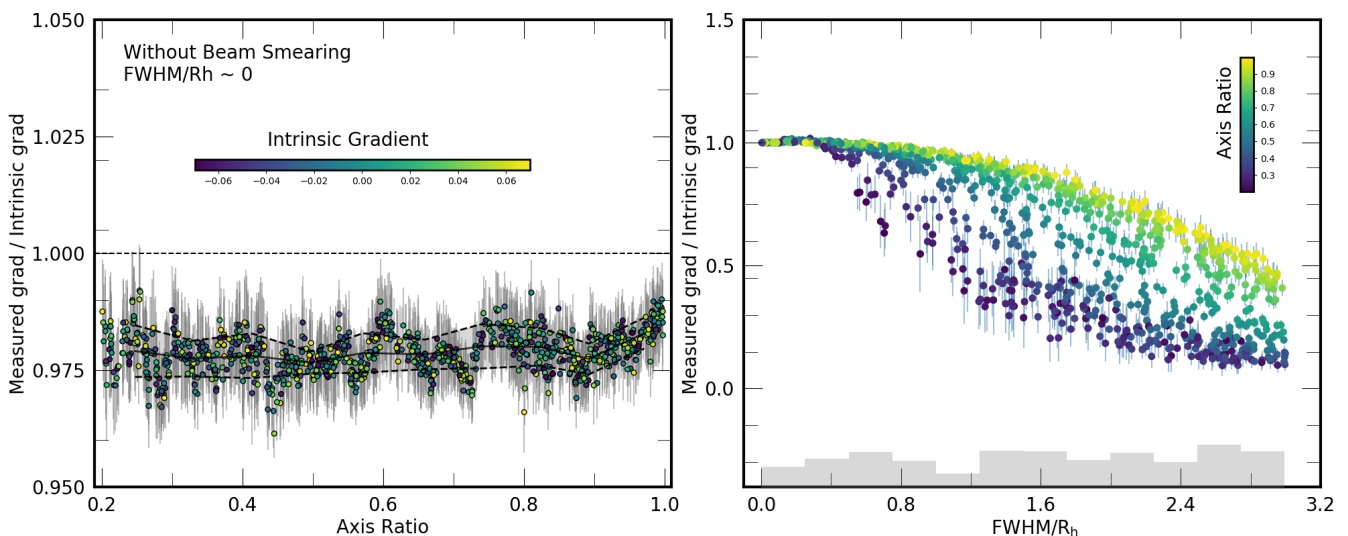
Figure B1. The ratio of measured metallicity gradient to intrinsic model gradient for 1000 mock galaxies of infinite signal to noise, as a function of axis ratio (left) and FWHM/R_h (right). We also show a histogram of FWHM/R_h values in the right hand panel. When the FWHM/$R_h \sim 0$, we find no dependence on the axis ratio of the galaxy with a median of ($\Delta Z/\Delta R$ measured)/($\Delta Z/\Delta R$ intrinsic) = 0.98 ± 0.01 with a scatter of 0.01. The offset from unity at all axis ratio is caused by the finite pixel sampling of the continuous distribution used to model the intrinsic gradient. When the FWHM/$R_h > 0$, we identify a strong dependence on our ability to recover the intrinsic gradient as a function of FWHM/R_h as well as axis ratio. For a fixed FWHM/R_h ratio, the metallicity gradient in a more edge on galaxy less well recovered than a more face-on galaxy.
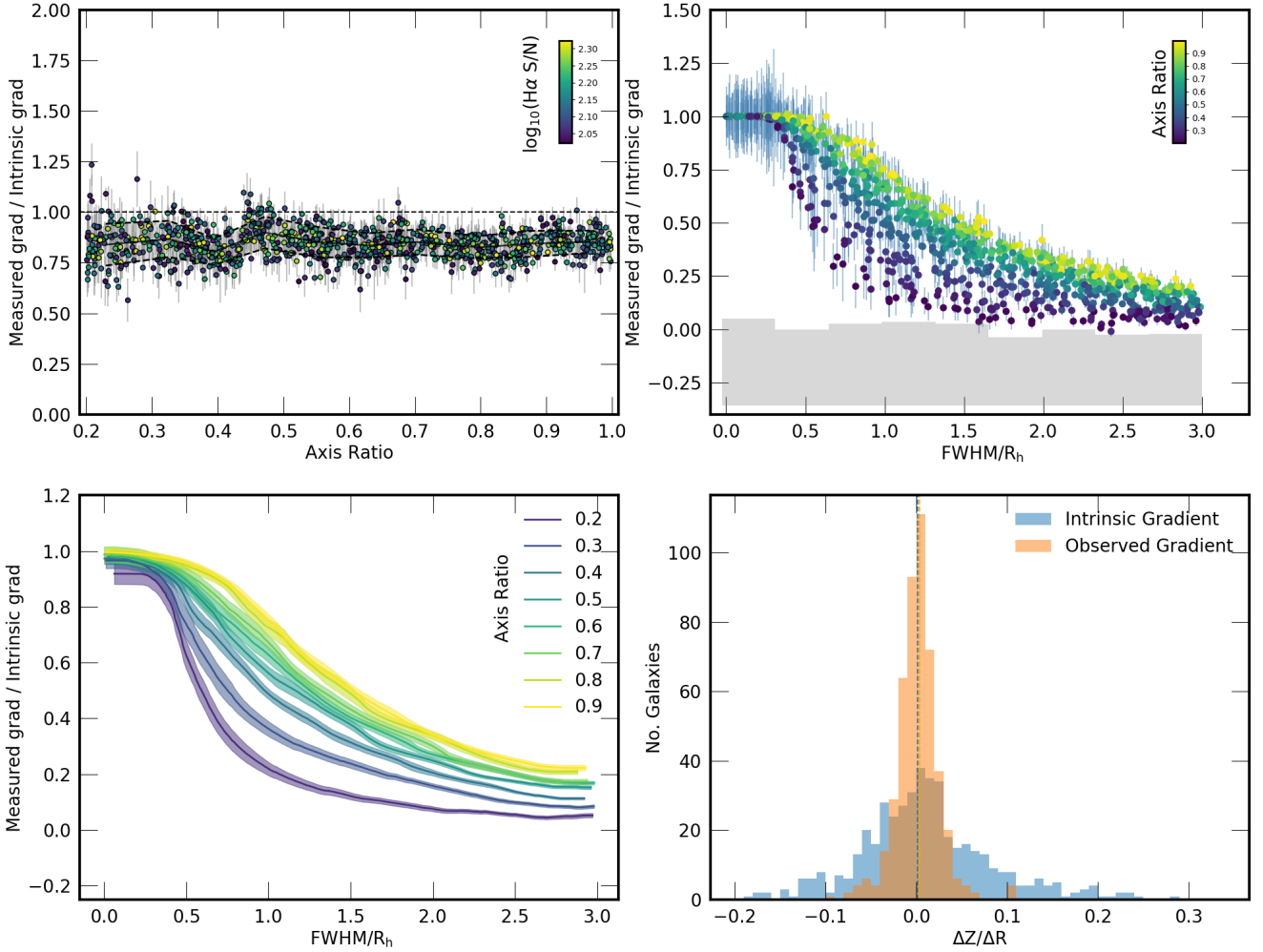
Figure B2. The ratio of measured metallicity gradient to intrinsic model gradient for 1000 mock galaxies with signal to noise comparable to the KMOS observations, as a function of axis ratio (left) and FWHM/R_h (right). We also show a histogram of FWHM/R_h values in the right hand panel. When the FWHM/R_h ~ 0, we find no dependence on the axis ratio of the galaxy with a median of $(\Delta Z/\Delta R$ measured $)/(\Delta Z/\Delta R$ intrinsic $) = 0.88 \pm 0.02$ with a scatter of 0.2. The larger scatter is driven by the variation in signal to noise between the models. We apply this correction factor to the metallicity gradients before modelling the impact of beam smearing. When the FWHM/R_h > 0, we identify a strong dependence on our ability to recover the intrinsic gradient as a function of FWHM/R_h as well as axis ratio. For a fixed FWHM/RR_h ratio, the metallicity gradient in a more edge on galaxy is less well recovered than for a more face-on galaxy, however with more scatter than the infinite signal to noise version. The bottom left panel shows an interpolation of the ratio of the measured metallicity gradient to intrinsic model gradients as a function of FWHM/R_h at fixed axis ratio. The shaded regions show the $1 - \sigma$ uncertainty on each correction curve derived from bootstrapping the uncertainty on the derived metallicity gradient. The bottom right panel shows a histogram of the observed metallicity gradient as well as the intrinsic, beam smearing corrected, metallicity gradient for the sample. The median observed metallicity gradient of the observational sample is $\Delta Z/\Delta R = 0.0005 \pm 0.0013$ dex kpc^{-1} with a scatter of 0.037. The median intrinsic metallicity gradient is $\Delta Z/\Delta R = 0.002 \pm 0.004$ dex kpc^{-1} with a scatter of 0.05.
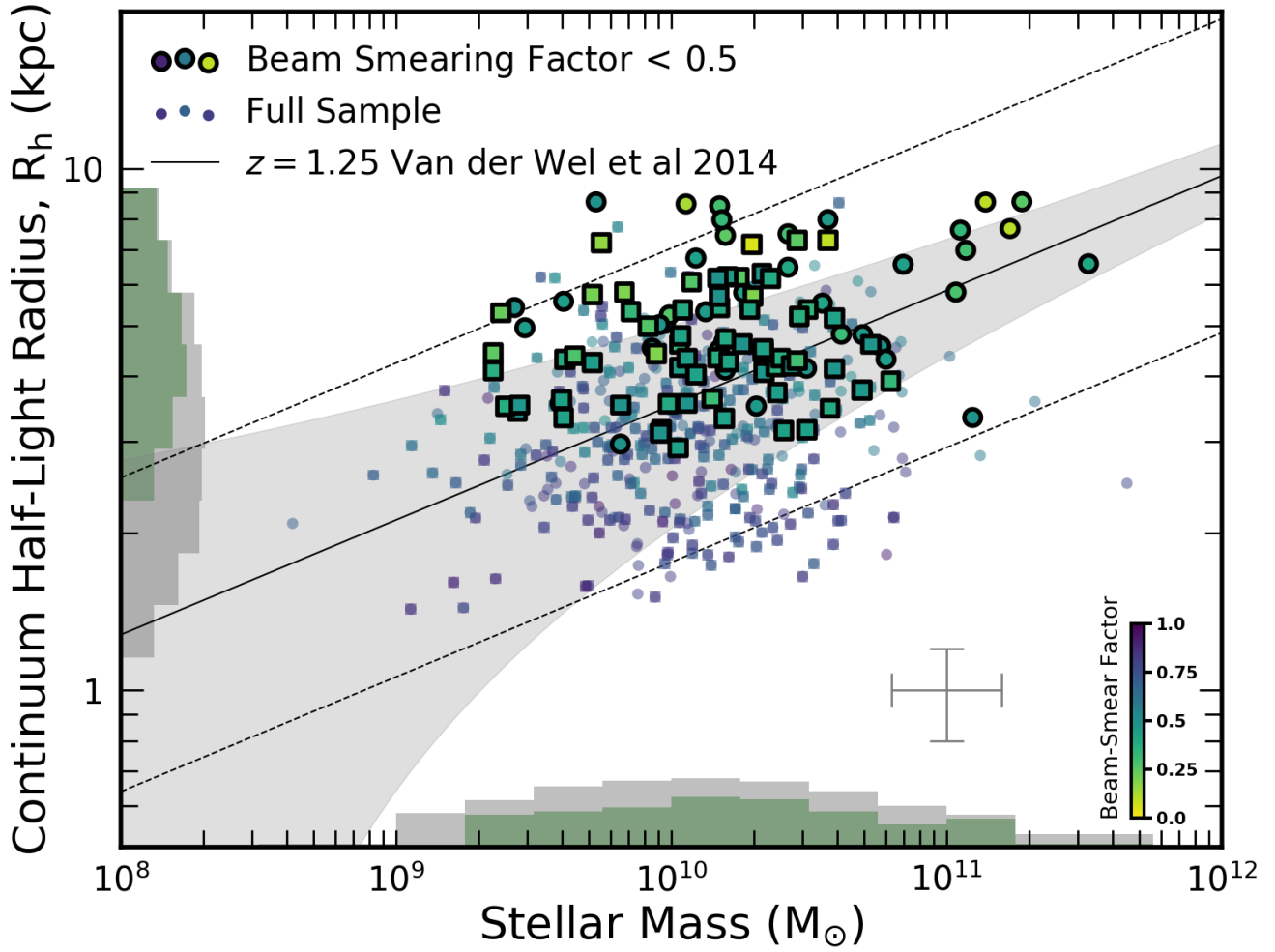
Figure B3. The stellar continuum half-light radius (R_h) as a function of stellar mass (M_*) for our sample at $z \approx 0.6 - 1.0$ (*squares*) and $z \approx 1.2 - 1.8$ (*circles*), coloured by the beam smearing correction factor derived for the galaxy. The median uncertainty on stellar mass and stellar continuum size are shown by the grey error bars in the lower right hand corner. We show histograms of both stellar mass and stellar continuum size on each axis. The solid line (and shaded region) indicate the mass-size relation (and uncertainty) for star-forming galaxies at $z = 1.25$ as derived by van der Wel et al. (2014). The dashed lines are a factor of two above and below the relation. The 98 galaxies with a beam-smearing correction factor to the metallicity gradient less than 50 per cent (black outlined points), have a similar stellar mass distribution to the overall sample whilst having larger continuum sizes, by definition.